Contrib Mineral Petrol (2005) 148: 582–601
DOI 10.1007/s00410-004-0624-9

ORIGINAL PAPER

Rainer Thomas · Hans-Jürgen Förster
Karen Rickers · James D. Webster

Formation of extremely F-rich hydrous melt fractions and hydrothermal fluids during differentiation of highly evolved tin-granite magmas: a melt/fluid-inclusion study

Received: 2 May 2004 / Accepted: 16 September 2004 / Published online: 16 November 2004

Abstract Quartz crystals from topaz–zinnwaldite–albite granites from Zinnwald (Erzgebirge, Germany) contain, in addition to primary and secondary fluid inclusions (FIs), abundant crystalline silicate-melt inclusions (MIs) with diameters up to 200 μm. These MIs represent various stages of evolution of a highly evolved melt system that finally gave rise to granite-related Sn–W mineralization. The combination of special experimental techniques with confocal laser Raman-microprobe spectroscopy and EMPA permits precise measurement of elevated contents of H_2O, F, and B in re-homogenized MIs. The contents of H_2O and F were observed to increase from 3 to 30 and 1.9 to 6.4 wt%, respectively, during magma differentiation. However, there is a second MI group, very rich in H_2O, with values up to 55 wt% H_2O and an F concentration of approximately 3 wt%. Ongoing enrichment of volatiles H_2O, F, B, and Cl and of Cs and Rb can be explained in terms of magma differentiation triggered by fractional crystallization and thus, is suggested to reflect elemental abundances in natural magmas, and not boundary-layer melts. Partitioning between melt and cogenetic fluids has further modified the magmatic concentrations of some elements, particularly Sn. The coexistence of two types of MIs with primary FIs indicates fluid saturation early in the history of magma crystallization, connected with a continuous sequestration of Sn, F, and B. The results of this study provide additional evidence for the extraordinary importance of the interplay of H_2O, F, and B in the enrichment of Sn during magma differentiation by decreasing the viscosity of and increasing the diffusivity in the melts as well as by the formation of various stable fluoride complexes in the melt and coexisting fluid.

Editorial Responsibility: J. Hoefs

R. Thomas (✉) · K. Rickers
GeoForschungsZentrum Potsdam,
Telegrafenberg, 14473 Potsdam, Germany
E-mail: thomas@gfz-potsdam.de
Tel.: +49-331-2881474

H.-J. Förster
Institute of Earth Sciences, University of Potsdam,
14415 Potsdam, Germany

K. Rickers
Hamburger Synchrotronstrahlungslabor HASYLAB
at Deutsches Elektronen-Synchrotron DESY, Notkestrasse 85,
22603 Hamburg, Germany

J. D. Webster
Department of Earth and Planetary Sciences,
A.M.N.H., Central Park West at 79th Street,
New York, 10989, USA

Introduction

Melt inclusions (MIs) are small blebs of silicate liquid that are trapped within growing phenocrysts at magmatic temperatures and pressures (Roedder 1984; Lowenstern 2003). Relatively stable and incompressible hosts such as quartz in silicic rocks act as pressure vessels, keeping most trapped MIs from degassing and preventing other mass flows into or out of the melt-inclusion system. Similar to what fluid inclusions (FIs) are for the study of hydrothermal processes, MIs yield a wealth of information on the origin, nature, and evolution of the trapped melt or magmatic processes (Roedder 1984, 2003). In the last years, many technical difficulties inherited in the early stages of the study of MIs were overcome and proper tools for the study of trapped portions of uncommonly volatile-rich melt phases in extrusive and intrusive rocks were developed. If correctly understood, MIs are the primary means of providing detailed information on the late evolution of magmas characterized by crystal/liquid equilibrium and the nature and amount of volatiles. Volatile components such as H_2O, F, Cl, B, and others largely control the rheological properties such as melt viscosity and affect magma crystallization temperature, thus they are the fundamental cause of magma ascent, liquid immiscibility, effervescence, expansion, and fragmentation (Lowenstern 2003).

This paper deals with the composition of MIs in quartz and of FIs in quartz and cassiterite from highly evolved, F- and H_2O-rich, topaz–albite–zinnwaldite Sn–W granites (Zinnwald, eastern Erzgebirge, Germany), and primarily discusses their H_2O and F contents. These MIs required special treatment during re-homogenization to avoid the loss of volatiles from the initially crystalline inclusions. Quartz grains from these granites contain a large number of MIs of widely different diameters, from about 1–200 μm (Fig. 1a), making them ideally suited for the development of methods to homogenize and analyze them. The paper complements a recent study of MIs from a chemically similar granite from Zinnwald that focused on major- and trace-element compositions (Webster et al. 2004). An outline of the magmatic evolution in the eastern Erzgebirge is provided by Štemprok et al. (2003).

The aims of the paper are threefold. First, it introduces a method for a more accurate determination of H_2O in re-homogenized silicate-MIs. The contents of H_2O, F, and several trace elements (Rb, Cs, Sn) were subsequently used to outline the igneous evolution of the Zinnwald magmatic-hydrothermal system. Second, it provides arguments for or against the "boundary-layer" (BL) effect (see Lowenstern 2003), which could, conceivably, be the origin of the non-representative enrichment of H_2O and some major and trace elements in MIs (Al, Na, Rb, Cs, B, Cl, F) and in FIs (Cu, Zn, Rb, Cs) in quartz of the cogenetic Sn–W mineralization. Finally, it shows that F became effectively partitioned from the late-stage melt into the ore-bearing fluid phase. This observation corroborates recent experimental results on the distribution of F and Cl between an F-rich melt and coexisting fluid (Webster et al. 2004), demonstrating that F has a greater influence on the extraction and transport of Sn in F–H_2O-rich magmas than implied from earlier experiments and thermodynamic calculations (e.g., Jackson and Helgeson 1985; Keppler and Wyllie 1991).

Sample characteristics

The topaz–albite granite sample TH212 represents a boulder collected about 1.3 km northeast of the village of Zinnwald (location Fuchshübel). The rock is pale gray with a light pink shade and contains about 33 vol% phenocrysts comprising smoky quartz up to 5 mm in diameter, albite, orthoclase, and different Li micas and muscovite. The quartz phenocrysts contain isolated feldspar crystals and aggregates of feldspar, mica, fluorite, topaz, and cryolite (Fig. 1c). The fine-grained groundmass is composed mainly of quartz, orthoclase, albite, micas, and topaz. Fluorite, rutile, cassiterite, zircon, xenotime, monazite, and pyrochlore are accessory phases.

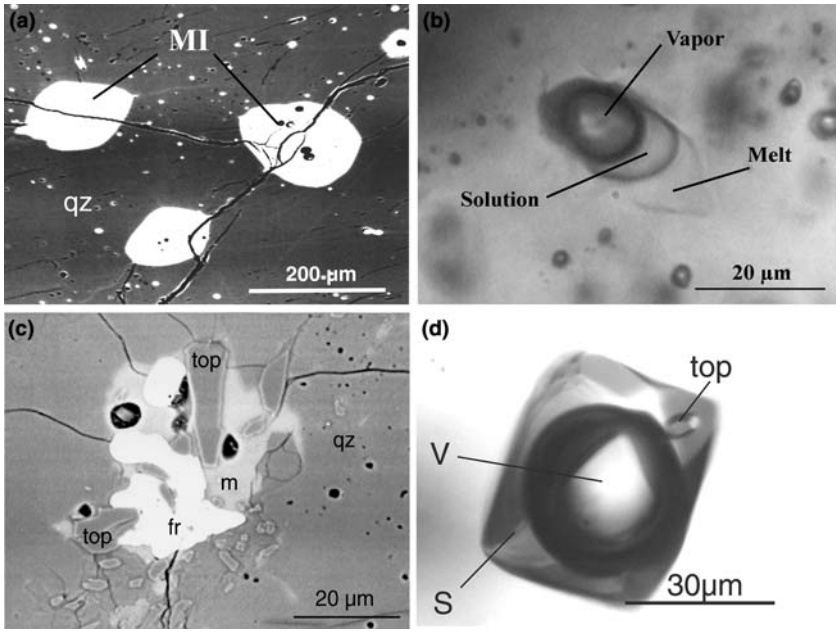

Fig. 1 Back-scattered electron images (**a** and **c**) and microphotograph (**b**) of MIs trapped in quartz in topaz–albite granite from Zinnwald, Erzgebirge. **a** Surface-polished, large homogeneous MIs prior to EMP analysis (no. 32 in Table 1), re-homogenized at ambient pressure and 905°C, **b** type-B MI in quartz, re-homogenized at 750°C and 1 kbar, **c** crystal-melt patch in quartz composed of topaz (*top*), fluorite (*fr*), and melt (*m*) showing that quartz, topaz, fluorite and melt coexisted at some stages of crystal growth. **d** Microphotograph of an FI in hydrothermal quartz from Zinnwald composed of topaz (*top*), boric acid-bearing solution (*s*), and vapor (*v*). **e** Re-homogenized type-B MIs in granite quartz. **f** A typical photomicrograph of an HDAC experiment in the SiO_2–Al_2O_3–Na_2O–K_2O–H_2O system showing droplets of silicate melt (*M*) in an aqueous fluid (*S*) and a vapor bubble (*V*) at 250°C (*upper photo*). The *lower photo* shows droplets of silicate melt (*M*) in an aqueous fluid (*S*) at 440°C. The partial homogenization temperature (glass + solution + vapor → glass + solution) is 337°C. The total homogenization occurs at 787°C in the solution according to the scheme (melt + solution → solution)

Fig. 1 (Contd.)

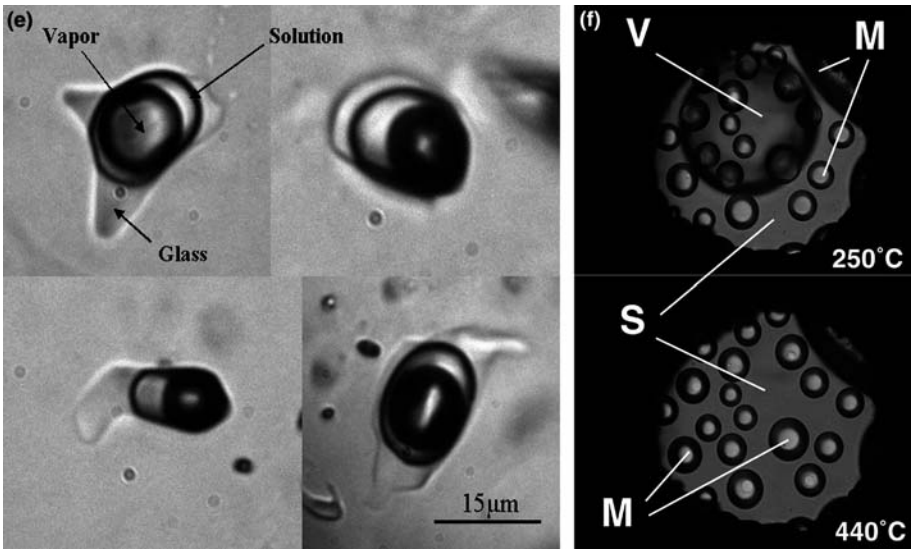

The quartz crystals are characterized by a myriad of tiny secondary FIs, mostly along trails, typically smaller than 10 μm, and crystalline MIs, with diameters ranging from 1 to rarely 200 μm (Fig. 1a). Large MIs may contain crystals of quartz, albite, K-feldspar, mica, topaz, fluorite, cryolite, and other, unidentified phases. In addition to "normal" MIs (type-A of Thomas et al. 2000, 2003), a second group of extremely H_2O-rich MIs (type-B, ibid), with diameters from 5 to 60 μm, occurs (Fig. 1e, after re-homogenization). These brownish inclusions are distinguished by the presence of a vapor bubble in a fine-grained mass of mica, topaz, and a liquid-H_2O solution. In several large inclusions of this group, small crystals (~3 vol%) of an REE-fluorocarbonate, probably bastnäsite, occur. Even more rare than MIs > 100 μm are glassy inclusions composed of a multiphase shrinkage bubble (5–10 vol%), a small crystal, liquid, and vapor.

Other samples investigated in this study (#1158 and #1159) come from Zinnwald-granite dikes crosscutting the Teplice rhyolite (see Webster et al. 2004, their Fig. 1). Both the bulk-rock composition and MI characteristics of these samples are indistinguishable from those of sample TH212.

To characterize the direct connection between the magmatic stage and the hydrothermal events forming the postmagmatic Sn–W ore deposit of Zinnwald we have studied two groups of primary FIs in a quartz crystal intergrown with cassiterite from the main stage of the deposit. The 3×1.5-cm large smoky quartz crystal is characterized by a small number of growth zones with FIs (~50 μm in diameter) with contrasting composition that were trapped at approximately the same temperature and pressure. The first FI group (Fig. 1d) is characterized by topaz daughter crystals and the second group by nahcolite. The FIs fulfill the criteria of an FI assemblage (FIA) according to Goldstein and Reynolds (1994).

Experimental and analytical techniques

Re-homogenization of crystalline melt inclusions

Melt inclusions in intrusive rocks such as the Zinnwald granites are small and completely crystalline and require heating to a homogeneous, daughter crystal-free glass prior to analysis by electron microprobe (EMP), ion microprobe (SIMS), or FTIR- and Raman spectroscopy. Owing to the slow melting kinetics of some minerals (e.g., feldspars), temperatures as high as 1,025–1,100°C are sometimes required to completely homogenize such inclusions. These temperatures are well above the trapping temperatures between about 570 and 810°C for the samples described here (see also Thomas and Klemm 1997). Unfortunately, heating to a temperature exceeding this trapping temperature can induce loss of H_2O and/or hydrogen by decrepitation, leakage, and diffusion, which is particularly critical for trapped melts containing H_2O in excess of 6 wt%. Consequently, H_2O concentrations measured in homogenized H_2O-rich MIs may be subject to large error, as has been demonstrated by Massare et al. (2002) for olivine-hosted MIs. Although probably being less critical, the true magmatic concentrations of F and B may also be underestimated, considering that both volatiles form highly mobile aqueous complexes. EMP-determined major-element compositions become increasingly imprecise as the extent of volatile loss increases during sample reheating (e.g., Devine et al. 1995; Morgan and London 1996).

Measurement of the partial homogenization temperature of the fluid phase inside MIs shows that leakage and partial decrepitation already takes place above the relatively low temperature of 400°C at fluid pressure. The loss of H_2O at T ≥400°C could be minimized by heating at a higher confining pressure and at a temperature that only minimally exceeds the

MI trapping temperature. Therefore, in this study, homogenization of MIs used for the determination of H_2O was performed at moderate pressures and temperatures of about 1,000 bars and 600–850°C, employing experimental designs described in the next but one three sections. However, even at these most optimal conditions, only small inclusions homogenized without signs of leakage (e.g., Student and Bodnar 1999; Student 2002).

Hydrothermal diamond-anvil cell (HDAC) experiments (reconnaissance studies)

During our inclusion work, we have seen that the so-called type-B MIs (Fig. 1b, e) are relatively widespread in the studied Zinnwald granite samples. Because of the decrepitation tendency of such MIs, the homogenization behavior could not be simply studied using conventional microscopic heating stages. Therefore, we have performed simple HDAC experiments simulating the behavior of the type-B MIs during heating and cooling.

For this we used an externally heated Bassett-type HDAC (Bassett et al. 1993; see also Veksler et al. 2002) with nonfluorescent diamond anvils. The inclusion volume was formed with an Re gasket with uncompressed thickness of 125 μm and a hole in the gasket of 400 μm in diameter. The sample chamber was filled with synthetic glass of peralkaline residual (PR) composition (33 vol%) and pure H_2O. The dry PR-glass has the following composition (in wt%): 75 SiO_2, 5 Al_2O_3, 10 Na_2O, and 10 K_2O. Before sealing the chamber, some H_2O was removed by leakage. Pressure is generated during heating because the sample follows an approximately isochoric path defined by the bulk density.

Cold-seal pressure vessel homogenization experiments

Small, polished thick-section chips (1-mm-thick) were loaded into an open Au capsule (30-mm long, 5-mm diameter) and placed in a horizontal, cold-seal pressure vessel. The vessel was pressurized with CO_2 to 1,000 bars, then moved into the preheated furnace. The experiments were performed at four different temperatures: 600, 650, 700, and 750°C and a heating time of 50 h. The used run time was constrained by kinetic experiments (cp. Thomas 1994a; Danyushevsky et al. 2002). During fast heating, the pressure was regulated to be constant at 1,000 bars for each experiment. After that, the vessel was removed from the furnace and quenched with cold air.

After quenching, the samples were removed from the pressure vessel, re-polished and mounted on glass disks for the determination of H_2O by confocal micro-Raman spectroscopy. Only completely homogeneous MIs were studied.

Hydrothermal rapid-quench homogenization experiments

Double-polished plates of quartz phenocrysts (1-mm-thick) were placed into an Au-capsule (5×30 mm) with a fixed amount of pure H_2O. The inclusions were re-melted at a temperature of 850°C and a pressure of 1,000 bars using the conventional hydrothermal rapid-quench technique. The run time of the unbuffered experiments was 24 h. After each run, the samples were quenched isobarically (see Thomas et al. 2000; Veksler and Thomas 2002). The rapid-quench technique was used to homogenize H_2O-rich type-B MIs to a homogeneous glass for Raman spectroscopic studies.

Homogenization experiments at ambient pressure

The heating and quenching experiments were performed using small, 500-μm-thick doubly-polished quartz chips placed in thin-walled evacuated quartz glass ampules and heated in a tubular furnace (Lenton Thermal Designs Ltd. with Eurotherm Controller, type 808). Temperatures are controlled by an Ni/Cr–Ni thermocouple with an accuracy of ±6°C or better.

A series of experiments were run at different temperatures between 800 and 1,040°C. Each experiment was held at run temperature for a constant duration of 20 h and for each experiment new quartz chips were used (e.g., Thomas 1994a; Webster et al. 2004). After heating, the samples were quenched in liquid nitrogen and examined under an optical microscope for complete homogenization. The samples from these experiments were used for EMP analysis, mainly because H_2O-rich glasses were observed to quickly decompose under the electron beam.

Electron-microprobe analysis

Chips with re-homogenized MIs were mounted on glass disks and polished under oil. They were analyzed for major and minor elements using CAMECA SX50 and SX100 EMPs. Analyses were performed in wavelength-dispersive mode under the following conditions: 15 kV acceleration voltage, 10 nA beam current, spot size of 10–40 μm, 40 s counting time for F using a multilayer PC1 crystal, 60–120 s for Sn, 40 s for Rb, Cs, and P and 20 s for other elements. Synthetic oxides and minerals were used as standards. Rb and Cs were calibrated with synthetic Rb-feldspar and pollucite ($CsAlSi_2O_6$) crystals. The accuracy of the EMP procedure was checked by analyzing chips of well-studied synthetic hydrous glasses and the Macusani glass; the agreement between predicted and measured values was within 10%.

Additionally, Rb and Sn contents were measured in approximately 100 totally homogenized MIs of known major-element composition using a high-resolution trace-element program from the Cameca SX100 software. The analytical conditions were: 20 kV acceleration

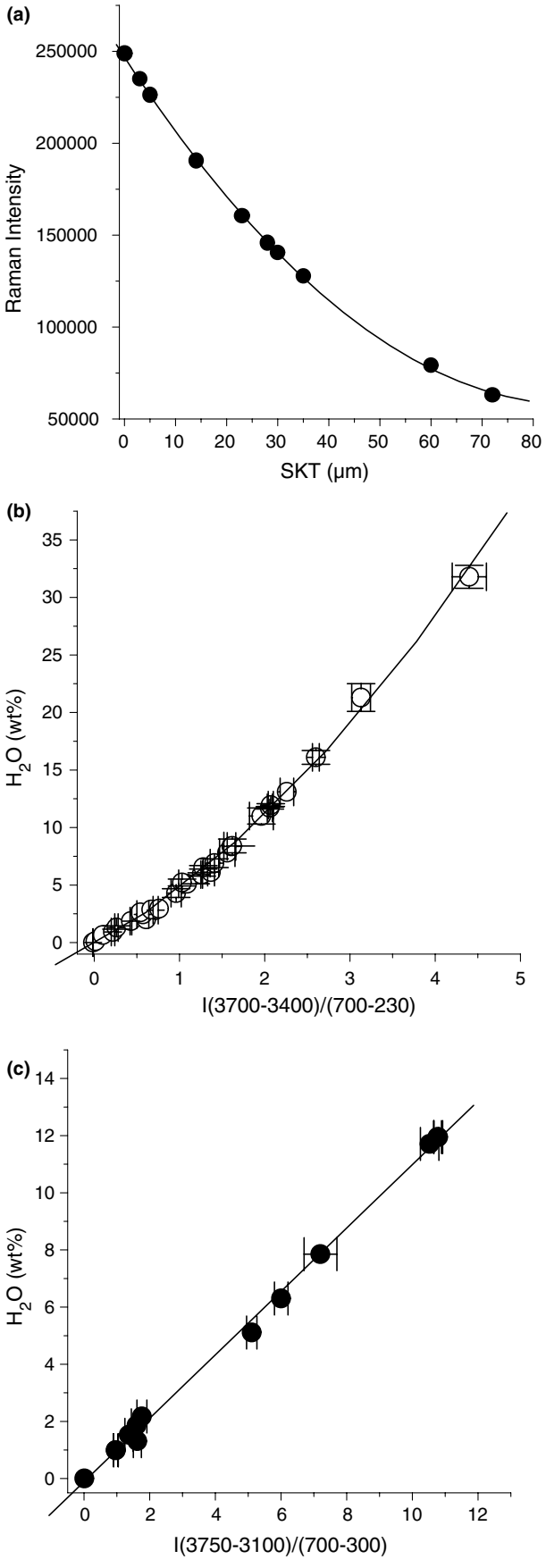

Fig. 2 **a** Changing of the Raman integral intensity in the high frequency region (3,100–3,750 cm^{-1}) with the depth (SKT in micrometer) of MIs (with a diameter of 60 μm) beneath the quartz surface. This correlation can be used to correct the measured reduced integral intensity obtained from MIs in depths between 10 and 100 μm. **b** Calibration curve for the determination of the bulk H_2O concentration (0–35 wt%) in MI with the Raman-spectroscopic technique (ratio method, see Thomas 2000). For the construction of this curve, 29 standard glasses were used. The polynomial regression gives: H_2O (wt%) = $0.732 \times I^2 + 4.102 \times I - 0.116$, $r^2 = 0.997$, SD = 0.35 (I integral intensity, r^2 correlation coefficient, SD standard deviation). To save time, we used different integration limits here (3,700–3,400 cm^{-1})/(700–230 cm^{-1}). **c** Working calibration curve for the H_2O determination with Raman spectroscopy using 13 glasses with different H_2O concentrations (0–13 wt%). The abscissa shows the used integral intensity ratio and the integral limits (3,750–3,100 cm^{-1})/(700–300 cm^{-1}). The linear regression gives: H_2O (wt%) = $1.10965 \times I - 0.10845$, $r^2 = 0.998$, SD = 0.24

voltage, 20 nA beam current, a spot size of 10 μm, and 300 and 600 s peak counting times for each element (see Thomas and Webster 2000). This technique was also used for the analysis of Cu, Zn, and Nb in a selection of MIs. The detection limit for Cu, Zn, Rb, Nb, and Sn was ~150 or ~60 ppm at counting times of 300 or 600 s.

In a limited number of homogenized MIs, B was analyzed in the trace-element mode at 10 kV and 40 nA using a PC2 pseudo-crystal (McGee et al. 1991) and the anti-contamination setup with liquid nitrogen. LaB_6 was used as an internal standard and synthetic glasses with B_2O_3 contents up to 20 wt% (Breitländer BR F2, BR 2/L, BR 4/l; CRM glass CZ 4001; synthetic glasses), cross-checked with Raman spectroscopy and EMP, were used as external standards (Thomas 2002a; Veksler and Thomas 2002). A counting time of 300 s at the peak, a shift of +500, and backgrounds between −5,200 and +8,000 were chosen. Analyses were also performed in the peak-area mode (60 s, 10,000 steps, five scans). Both methods yielded corresponding results. The lower limit of detection for B was 0.06 wt%.

Confocal laser Raman-microprobe spectroscopy

Raman-microprobe spectroscopy was used to determine the concentration of H_2O in homogenized MIs and to measure the concentration of H_3BO_3 in the H_2O-rich fluid and type-B MIs (see further below). This technique also was applied to identify daughter crystals other than halite and sylvite in the FIs, as well as to identify mineral phases like fluorite (320 cm^{-1}), cryolite (520 cm^{-1}), Y-REE fluorite, topaz (238, 266, 285, and 3,636 cm^{-1}), albite (503 cm^{-1}) and others in polished rock samples (in brackets: characteristic Raman bands).

Water concentrations were measured following the procedure described in Thomas (2000). The Raman probe consisted of a Dilor XY Laser Raman Triple 800 mm spectrometer equipped with an Olympus optical microscope and a long working distance 80x

objective. Spectra were collected with a Peltier cooled CCD detector.

The 488-nm line of a Coherent Ar^+ Laser Model Innova 70-3 and a power of 450 mW of the argon laser were used for sample excitation. The method employed in this study measures the ratio of the integral intensity of the asymmetric O–H stretching band between 3,100 and 3,750 cm^{-1} and the asymmetric broad band in the 490 cm^{-1} region between 300 and 700 cm^{-1}. The method works with a calibration curve, taken from glass standards with different H_2O contents. This "ratio method" eliminates sampling problems and reduces systematic errors and irreproducible instrumental variations.

The confocal capability of the Raman microprobe greatly enhanced the depth resolution allowing measuring MIs to a depth of about 100 μm in the quartz host. Confocal microscopy uses a pinhole, placed in the back image plane of the microscope objective, to block light from outside the focal plane (Tabaksblat et al. 1992). In this way, the signal from the small volume of interest can be studied with minimal interference from the surrounding material. The applied confocal pinhole size was 150 μm in diameter. Each spectrum was collected ten times, with a counting time of 50 s for each accumulation.

The highest-quality spectra were obtained from excitation volumes of trapped glass that are nearest to the polished surface of the sample. The Raman signal from depths >10 μm beneath the surface is significantly reduced, and a simple correction procedure must be applied. For a totally homogenized MI (700°C, 1,000 bar) with a diameter of 60 μm at an initial depth of about 70 μm, step-wise polishing (nine steps) brought the MI to the sample surface, and the following correction equation for the Raman intensity (I) was obtained (Fig. 2a):

$$I = 24.532 \times \mathrm{SKT}^2 - 4308.04 \times \mathrm{SKT} + 247,356,$$

$$r^2 = 0.9996,\ \mathrm{SD} = 1,154$$

(SKT—microscope scale (in μm), r—correlation coefficient, SD—standard deviation of I).

If no small FI is located between the polished surface and the MI, inclusions up to a depth of 100 μm could be analyzed with sufficient accuracy (see Thomas 2000; Chabiron et al. 2003). Raman peak intensities for H_2O were calibrated using 29 synthetic granite, haplogranite, and albite glasses and natural glass samples of known composition, which covered a range between 0 and 33 wt% H_2O (Fig. 2b, c). For calibration, the H_2O contents of most of these glasses were determined by Karl–Fischer titration (see Thomas 2000, 2002b). Values greater than 20 wt% H_2O in glass were obtained from type-B MIs totally homogenized with the rapid-quench technique. After Raman measurements and following disintegration of the metastable inclusion glass into stable glass and liquid H_2O phase, the bulk H_2O concentration was obtained by Raman measurements and volume estimation.

The concentrations of H_3BO_3 in FIs and type-B MIs were determined using the Raman band at 876 cm^{-1} (see Thomas 2002a). The sample excitation was performed using the 514 or 488-nm lines of an Ar ion laser (Coherent Innova 70-3) with a power up to 1,500 mW. Frequencies of the Raman lines were calibrated by monitoring the position of the principal plasma lines in the argon ion laser.

Fluid-inclusion microthermometry

A calibrated LINKAM THMS 600 heating and freezing stage, together with TMS92 temperature programmer and LNP2 cooling system, were used to determine the salinity and liquid-vapor homogenization temperature of hydrothermal FIs in quartz and cassiterite. Calibration was done using synthetic FIs of known density and composition and with various melting-point standards (In, Sn, Pb, potassium dichromate). The measurements were performed under argon. The standard deviation depends on absolute temperature and is always better than ±2.5°C for temperatures greater 100°C and ≤ 0.2°C for cryometric measurements at temperatures <20°C. Chips consisted of 300-μm-thick quartz and cassiterite plates polished on both sides.

Synchrotron radiation X-ray fluorescence (XRF) analysis

Synchrotron radiation XRF analysis was performed at the fluorescence beamline L of the Hamburger Synchrotronstrahlungslabor HASYLAB at the Deutsches Elektronen-Synchrotron DESY, Germany. The synchrotron radiation at beamline L originates from a bending magnet of DORIS III, a second-generation synchrotron source. A double-crystal NiC multilayer monochromator was used to monochromatize the polychromatic bending magnet continuum at 38 keV providing a high flux. This energy was chosen to optimize lower limits of detection of Cs via K-shell excitation. On the one hand, the excitation energy was slightly above the absorption edge of the Cs K lines and on the other hand, energies were higher to keep the Cs K-emission lines in an area of low background, i.e., separated from the Compton scatter contribution of the sample. A 2-mm-Al absorber was chosen for reducing the background in the low-energy part of the spectrum, also with the intention to increase peak to background ratios and, accordingly, to decrease the lower limits of detection. A single bounce capillary (Bilderback and Huang 2001) designed for beamline L (Falkenberg et al. 2003) was used to focus the synchrotron beam collimated to a cross-section of 400×400 μm^2 by tungsten cross-slits to a spot of 11 μm on the sample. The

Table 1 MIs in quartz: microprobe analyses (wt%, recalculated to a sum of 100/water-free and sorted in order of ascending F concentration)

No.	SiO_2	TiO_2	B_2O_3	Al_2O_3	FeO	MnO	MgO	CaO	Na_2O	K_2O	Rb_2O	Cs_2O	F	Cl	P_2O_5	ASI	*n*	H_2O
TH212	74.1	d.l.	NA	14.9	0.62	0.05	0.04	0.15	3.62	4.65	0.27	0.07	0.31	0.02	0.01	1.30	1	–
TH212	75.2	0.05	NA	13.9	1.36	0.23	0.10	d.l.	3.73	4.42	0.29	NA	0.60	0.08	d.l.	1.26	1	–
# 1158	73.9	d.l.	NA	14.9	0.75	0.05	0.04	0.33	4.05	4.83	0.28	0.01	0.61	d.l.	0.01	1.18	1	–
# 1159	72.9	d.l.	NA	15.1	0.51	0.06	0.01	0.41	4.47	4.48	0.56	0.02	0.93	d.l.	0.01	1.14	1	–
5	67.1	d.l.	NA	19.4	0.31	0.15	d.l.	0.67	4.47	6.07	0.67	d.l.	1.16	d.l.	d.l.	1.25	1	12.5
6	73.4	0.06	NA	15.2	0.65	0.15	0.06	0.42	2.66	5.01	0.80	NA	1.56	d.l.	d.l.	1.38	1	5.8
7	78.1	0.05	NA	10.5	3.61	0.23	d.l.	d.l.	1.93	3.56	0.40	NA	1.56	0.03	0.11	1.44	1	3.0
8	70.9	0.06	NA	16.9	0.88	0.12	d.l.	0.05	3.76	4.73	0.79	d.l.	1.78	d.l.	d.l.	1.42	1	3.8
9	75.4	0.06	NA	11.9	3.24	0.14	0.02	0.03	2.42	4.23	0.44	d.l.	1.92	0.20	d.l.	1.34	3	8.2
10	75.5	0.07	NA	11.7	3.64	0.18	d.l.	0.09	2.67	3.69	0.44	NA	2.03	d.l.	d.l.	1.33	1	8.4
11	72.7	d.l.	NA	13.4	2.42	0.80	d.l.	0.08	2.97	4.24	0.95	0.18	2.19	d.l.	d.l.	1.31	1	9.3
Pyknite	73.0	d.l.	1.06	11.1	3.94	0.25	d.l.	d.l.	1.17	6.28	0.68	d.l.	2.35	d.l.	0.04	1.22	1	13.9
13	77.7	d.l.	NA	10.9	0.16	0.24	d.l.	0.05	1.74	3.90	0.83	1.76	2.55	0.25	d.l.	1.31	1	9.4
14	70.5	d.l.	NA	14.6	0.53	0.90	d.l.	d.l.	2.98	5.39	0.96	1.37	2.64	0.08	d.l.	1.24	1	12.9
15	72.6	0.05	NA	12.4	2.68	0.83	0.03	0.10	2.64	4.91	1.01	NA	2.65	0.02	0.04	1.20	2	15.3
16	75.1	d.l.	NA	13.7	0.45	0.09	d.l.	0.14	3.16	4.04	0.44	0.06	2.66	0.12	0.04	1.36	1	6.8
17	73.0	0.03	NA	14.0	0.15	0.12	d.l.	0.15	2.89	5.98	0.66	d.l.	2.86	0.04	d.l.	1.18	1	15.9
18	76.3	d.l.	NA	12.4	0.42	0.14	d.l.	0.16	2.77	4.33	0.50	d.l.	2.87	d.l.	d.l.	1.26	1	11.9
19	77.5	d.l.	NA	11.0	1.02	0.41	d.l.	d.l.	2.41	3.68	0.80	0.06	3.07	d.l.	0.03	1.31	1	9.8
20	76.0	d.l.	NA	12.2	0.93	d.l.	d.l.	0.24	2.47	4.48	0.36	d.l.	3.13	0.03	d.l.	1.28	1	11.3
21	72.8	d.l.	NA	11.7	2.55	0.64	0.08	d.l.	2.19	5.73	1.19	NA	3.17	d.l.	d.l.	1.12	4	19.2
22	67.6	0.06	NA	15.5	1.41	0.48	d.l.	0.44	3.49	5.40	1.98	0.44	3.20	d.l.	d.l.	1.14	1	18.3
23	72.9	d.l.	NA	11.7	2.48	0.37	d.l.	d.l.	2.07	5.58	1.23	0.24	3.50	d.l.	d.l	1.14	1	26.9
24	75.6	d.l.	0.72	11.7	0.44	d.l.	d.l.	0.14	2.90	4.32	0.52	d.l.	3.52	0.04	d.l.	1.17	1	25.5
25	73.0	d.l.	NA	13.2	0.53	0.22	d.l.	0.12	2.00	6.55	0.76	NA	3.53	0.13	d.l.	1.19	2	24.0
26	71.9	d.l.	NA	12.1	2.49	0.51	d.l.	d.l.	2.07	5.70	1.27	0.28	3.70	d.l.	d.l.	1.17	1	25.5
27	73.2	d.l.	NA	13.1	0.58	0.11	d.l.	0.14	3.34	5.15	0.58	d.l.	3.75	0.03	d.l.	1.12	1	28.0
28	66.2	d.l.	NA	17.5	0.53	0.14	d.l.	0.22	4.25	6.59	0.67	0.16	3.78	0.05	d.l.	1.17	1	25.5
29	72.2	0.04	NA	13.4	0.6	0.05	d.l.	0.02	2.16	6.80	0.82	0.06	3.79	0.11	0.04	1.17	1	25.4
30	70.9	d.l.	NA	12.1	3.44	0.62	d.l.	0.09	2.39	5.35	1.02	0.25	3.81	d.l.	d.l.	1.15	1	26.4
31	67.7	d.l.	NA	13.9	3.62	0.73	d.l.	0.02	3	6.03	0.99	0.15	3.83	d.l.	d.l.	1.15	1	26.4
32	67.3	0.03	2.16	13.3	2.71	0.89	0.02	0.14	2.52	5.99	0.87	0.14	3.86	0.04	d.l.	1.16	19	25.7
33	69.4	d.l.	NA	13.5	2.44	1.05	d.l.	d.l.	2.52	6.16	0.85	0.11	3.86	d.l.	d.l.	1.20	1	23.9
34	70.5	0.06	0.8	11.5	3.57	0.35	d.l.	0.29	2.22	3.90	2.19	0.44	3.89	0.24	0.04	1.18	3	24.7
35	69.8	0.04	NA	12.8	3.17	0.70	d.l.	0.02	2.70	5.76	1.01	0.14	3.93	d.l.	d.l.	1.13	1	27.6
36	66.6	0.03	0.71	15.8	0.78	0.12	d.l.	1.40	2.91	6.66	0.63	0.36	3.93	d.l.	0.08	1.05	4	31.9
37	68.5	d.l.	NA	13.8	3.26	0.72	d.l.	d.l.	2.38	6.12	1.04	0.16	3.97	d.l	d.l.	1.24	1	21.8
38	70.0	0.06	NA	13.5	2.84	0.14	d.l.	d.l.	2.16	6.32	0.72	d.l.	4.07	0.14	d.l.	1.25	2	20.7
39	74.3	d.l.	NA	13.3	0.32	0.11	d.l.	0.18	3.52	3.83	NA	NA	4.17	0.22	d.l.	1.29	13	18.5
40	65.7	0.02	1.12	13.6	2.74	0.91	d.l.	0.15	3.79	6.3	0.91	0.14	4.25	0.31	0.03	0.98	30	35.8
41	73.4	d.l.	NA	13.4	0.33	0.10	d.l.	0.16	3.52	3.87	0.41	0.08	4.43	0.32	d.l.	1.27	30	19.8
42	66.0	d.l.	NA	14.5	1.08	2.19	d.l.	0.99	2.73	7.43	0.56	d.l.	4.48	d.l.	0.03	0.99	1	35.4
43	69.7	0.22	NA	15.2	0.66	0.32	0.02	d.l.	2.3	6.15	0.77	d.l.	4.48	0.15	d.l.	1.40	1	12.6
44	68.8	0.13	NA	10.4	6.07	0.45	d.l.	d.l.	4.19	3.32	2.08	NA	4.50	0.05	d.l.	0.89	2	40.8
45	71.7	d.l.	NA	14.4	0.74	0.06	d.l.	0.13	2.88	4.69	0.45	0.14	4.58	0.08	d.l.	1.39	1	13.2
46	73.4	d.l.	NA	13.6	0.34	0.09	d.l.	0.14	3.55	3.93	NA	NA	4.66	0.28	d.l.	1.31	17	17.5
47	70.7	d.l.	NA	14.4	0.80	0.13	d.l.	0.17	2.56	5.20	0.74	0.28	4.67	0.25	d.l.	1.35	8	15.2
48	70.3	d.l.	NA	15.5	0.62	0.08	d.l.	0.20	2.93	5.15	0.42	NA	4.70	d.l.	0.03	1.41	6	12.1
49	66.3	d.l.	NA	13.8	0.82	2.13	d.l.	1.84	2.63	7.17	0.54	0.06	4.73	0.03	d.l.	0.87	1	41.7
50	70.4	d.l.	NA	15.3	0.55	0.09	d.l.	0.20	2.92	5.25	0.46	NA	4.74	0.10	d.l.	1.38	5	14.0
51	70.5	0.03	NA	15.4	0.63	0.08	d.l.	0.20	2.91	5.12	0.42	NA	4.75	d.l.	0.03	1.41	5	12.3
52	70.1	d.l.	0.12	15.1	0.64	0.09	d.l.	0.20	2.83	4.94	0.84	NA	4.96	0.10	d.l.	1.40	3	13.0
53	71.2	d.l.	NA	14.8	0.56	0.12	d.l.	0.22	2.59	4.95	0.45	d.l.	4.98	0.07	d.l.	1.44	1	10.4
54	70.8	d.l.	0.12	15.3	0.64	0.09	d.l.	0.20	2.86	4.99	NA	NA	5.01	0.10	d.l.	1.46	15	9.4
55	64.9	d.l.	NA	16.8	0.41	0.24	d.l.	0.08	4.02	3.72	1.79	2.87	5.06	0.14	d.l.	1.31	1	17.7
56	68.8	d.l.	NA	15.9	0.69	0.09	d.l.	0.18	3.28	4.99	0.73	0.11	5.10	0.09	d.l.	1.37	24	14.2
57	68.9	d.l.	NA	15.8	0.73	0.09	d.l.	0.18	3.28	4.99	0.43	NA	5.10	0.09	d.l.	1.39	24	13.1
58	70.1	d.l.	NA	15.8	0.65	0.09	d.l.	0.19	2.69	5.10	NA	NA	5.25	d.l.	0.05	1.54	3	5.1
59	69.5	d.l.	NA	15.1	0.65	0.86	d.l.	d.l.	2.40	5.22	0.92	d.l.	5.26	d.l.	d.l.	1.49	1	7.5
60	70.3	d.l.	NA	15.4	0.62	0.19	0.02	0.25	2.50	4.77	0.42	0.06	5.41	0.08	0.04	1.54	1	5.0
61	61.8	d.l.	NA	15.8	0.82	1.09	d.l.	d.l.	7.25	6.61	1.16	d.l.	5.45	d.l.	d.l.	0.80	1	45.7
62	62.1	0.05	NA	15.0	0.19	1.11	d.l.	d.l.	7.69	7.05	1.18	d.l.	5.51	d.l.	0.04	0.72	1	50.3
63	59.1	0.04	NA	15.5	0.22	0.54	d.l.	0.03	7.20	6.57	2.10	2.73	5.54	0.41	0.06	0.73	3	49.5
64	69.1	0.04	NA	15.5	0.15	0.85	d.l.	d.l.	2.36	5.38	0.90	d.l.	5.66	d.l.	0.03	1.52	1	6.2
65	64.9	0.06	NA	18.0	0.40	0.30	d.l.	d.l.	3.00	6.23	0.84	d.l.	5.72	0.03	d.l.	1.48	2	8.2
66	69.7	d.l.	NA	12.1	0.40	0.07	d.l.	0.13	6.19	5.72	NA	NA	5.72	0.05	d.l.	0.73	1	49.9
67	69.1	0.06	NA	15.8	0.10	0.43	0.02	d.l.	2.70	5.00	0.82	d.l.	6.02	d.l.	d.l.	1.53	1	5.5

Table 1 (Contd.)

No.	SiO_2	TiO_2	B_2O_3	Al_2O_3	FeO	MnO	MgO	CaO	Na_2O	K_2O	Rb_2O	Cs_2O	F	Cl	P_2O_5	ASI	*n*	H_2O
d.l. (wt%)	0.03	0.03	0.06	0.04	0.07	0.05	0.02	0.02	0.03	0.02	0.04	0.06	0.08	0.03	0.03			

Analyses 1–4: whole rock samples
H_2O (last column) – estimated water concentration using data from Table 3
For the analyses no. 39, 54, and 57, we have determined 0.25, 0.39, and 0.41 wt% Li_2O, respectively. Li was determined by SIMS at the Woods Hole Oceanographic Institution, MA, USA (see Webster et al. 2004)
d.l. detection limit; *NA* not analyzed; *n* number of re-homogenized MIs, analyzed by EMP; *ASI* aluminum saturation index (moles $Al_2O_3/[CaO + Na_2O + K_2O + Rb_2O + Cs_2O]$)

intensities of fluorescence and scatter from the sample were recorded by an energy-dispersive HPGe detector (GRESHAM Gemini 30) of 30 mm^2 active area. The semiconductor detector was placed at 90° to the incoming linear polarized X-ray beam to minimize the intensity of the scattering. The angle between beam and sample versus sample and detector was 45° each in order to minimize the path length of X-rays in the sample. For single inclusion analysis, quick area scans, with 10-μm-step sizes in both directions and an acquisition time between 10 and 30 s-per-point, were performed for positioning. Afterwards, analysis of single inclusions was performed with sample times of 1,200 s. Quantification of the inclusion data was performed using Monte Carlo simulations following the procedure described in Rickers et al. (2004). This method was employed to analyze ten trace elements (Fe, Cu, Zn, Cd, Ag, Sn, Sb, As, Rb, Cs) in a selection of FIs in hydrothermal quartz from the main stage of Sn–W mineralization in the Zinnwald deposit. Results were tested for accuracy and precision in two steps (e.g., Rickers et al. 2004): (1) area scans of synthetic glass standards yielded an accuracy of generally better than 20% for all elements with Z between 37 and 92. The standard deviation of the area-scan measurements was better than 7%, whereas repeatability of single-point measurements was better than 0.5%. (2) single-point measurements of synthetic inclusions in quartz yielded an accuracy of better than 20% for concentrations well above the lower limit of detection (test elements: Rb and Cs), and still better than 30% for concentrations close to the lower limit of detection (test elements: Sn and Cu), with a lower reproducibility of 20% and a repeatability of 6%.

Results

Geochemistry and mineralogy of the granites

The MI-containing granites are highly evolved, peraluminous topaz–albite–zinnwaldite Sn–W granites rich in F, Rb, and Cs, but poor in P (Table 1). The magmatic concentrations of many elements are difficult to determine owing to extensive, high- to low-temperature alteration, which is largely responsible for compositional differences observed between the three samples (TH212, #1158, #1159) listed in Table 1. Of the elements of interest for this study, alteration-induced differences relate to aluminum saturation index (ASI; 1.30 vs. 1.12), F (0.31 vs. 0.93 wt%), and Sn (148 vs. 74 ppm).

The granites contain various F minerals. Topaz (≥19.8 wt% F) occurs in the outermost growth zone of quartz phenocrysts, together with F-rich zinnwaldite (~7.2 wt% F), demonstrating that the F concentration in the melt increased during quartz growth. Other F species comprise magmatic fluorite up to 100 μm in diameter, cryolite (~20 μm), and spherical crystals of a Y-REE fluorite[1] up to 100 μm in diameter. The quartz phenocrysts of all three studied topaz–albite granite samples from Zinnwald (#1158, #1159, TH 212) contain the same Y-REE fluorite crystals, demonstrating the similarity of the studied granites. Some MIs show the coexistence of quartz, topaz, fluorite, and silicate melt (see Fig. 1c), in accordance with experimental data on F-rich granite systems (Dolejš and Baker 2004). In contrast to Sn-bearing peraluminous, phosphorous-rich granites from the central and western Erzgebirge (Thomas et al. 2003), tourmaline is extremely rare in our samples. Only two small crystals of blue tourmaline were observed isolated in the quartz phenocrysts. Some isolated crystals of muscovite in quartz contain 1.3 ± 0.4 wt% B_2O_3 ($n = 33$). Boromuscovite occurs as small crystals in some MIs, especially in the type-B MIs.

The average composition of isolated feldspar grains trapped in quartz phenocrysts, which remained unaffected by fluid-induced alteration (plagioclase: $Ab = 0.864$, $Or = 0.063$, $An = 0.070$; K-feldspar: $Ab = 0.379$, $Or = 0.617$, $An = 0.004$), indicates a low, concordant equilibrium temperature of 627°C (at 1 kbar) employing the thermometer of Fuhrman and Lindsley (1988). This temperature is similar to the beginning-of-melting temperature of the MIs of 652 ± 12°C (Thomas 1994b). A small number of MIs shows a significantly lower beginning-of-melting temperature of 572 ± 16°C (Thomas 1989; R. Thomas, unpublished data). With these temperatures, the entrapment pressure estimated from the intersection of the isochores for magmatic FIs (see Webster et al. 2004) with the experimentally determined granite solidus is $1{,}140 \pm 200$ bar (see also Audètat and Pettke 2003).

Generally, the primary mineral association of the studied samples is severely affected by postmagmatic alteration processes such as albitization and greisenization. The unaffected mineral association is preserved as

[1] Results on the new Y-REE fluorite will be presented elsewhere.

isolated mineral clusters in the quartz phenocrysts. In addition, idiomorphic water-clear albite, fluorite, topaz, Rb-rich mica, boromuscovite, and cryolite are hosted in quartz phenocrysts. A striking feature is the presence of up to 60×30 μm large crystals of rubidian leucite in quartz with the empirical formula

$(K_{0.64}Rb_{0.22}Na_{0.13}Cs_{0.01})(Al_{0.96}Fe_{0.03})Si_2O_6$

The formation of rubidian leucite in a granitic environment requires that part of the melt system must have evolved to strongly peralkaline conditions.

Homogenization behavior of the melt and fluid inclusions in granite quartz

Melt inclusions in quartz of the topaz–albite–zinnwaldite granite are usually crystalline, mostly opaque, and consist of a mixture of small crystals and an often-deformed vapor bubble. Two different silicate MIs can be distinguished according to the bubble volume: (1) "normal" MIs with a bubble volume of about 10–20% (type-A inclusions) and (2) volatile-rich MIs with a larger bubble and/or a visible fluid phase (type-B inclusions). Depending on the volatile content, MIs can homogenize in two different ways: (1) to an aluminosilicate-rich liquid (glass at RT) and (2) into an H_2O-rich solution. Generally, type-A MIs homogenize according to the first way and type-B MIs according to the second way.

Because of decrepitation tendency of H_2O-rich type-B MIs, the homogenization behavior could not be studied directly. However, to demonstrate this behavior, we have performed a couple of HDAC experiments using synthetic glass of PR composition. For the partial homogenization temperature (glass + solution + vapor → glass + solution) of such experiment we determined, after some recycling, a value of 337°C, which define the density of the isochore. Total homogenization in the solution occurs at 787°C according to the scheme (melt + solution → solution) – see Fig. 1f.

In further experiments, we have varied the PR-glass amount to demonstrate the different homogenization behavior depending on the glass-solution ratio. The results of these experiments will be presented in a forthcoming publication (I. Veksler et al., in preparation). By reducing SiO_2 and addition of F, Cl, and B to the "peralkaline residual glass," the total homogenization temperature can be reduced dramatically (see Thomas et al. 2003). From these experiments, the "real" type-B MIs should show the same liquid–liquid equilibrium behavior at high temperatures.

An important observation is that the size of the type-A MIs increases with F concentration. This dependence is probably the result of the decrease in melt viscosity and changing dihedral angles (McKenzie 1985) with increasing H_2O and F concentration.

In addition to the two MI types, coeval FIs occur. These FIs are mostly composed of a concentrated solution, with boric acid and different daughter phases such as halite, boromuscovite and others, as well as a vapor bubble. Phase changes and the homogenization behavior under controlled conditions could be observed only sometimes, because of the tendency of decrepitation and/or leakage at low temperature.

Composition of the melt inclusions

Most microprobe and Raman data were obtained from totally homogenized type-A MIs (Fig. 1a) which are presented in Table 1. Inclusions of type-B were difficult to analyze with microprobe techniques owing to their small diameter of < 15–20 μm and their instability under the electron beam (Fig. 1e). Only a small couple of type-B MIs could be analyzed (analyses with ASI ≤ 1.1 in Table 1). However, it was possible to determine the B content in the liquid phase of type-B inclusions by Raman spectroscopy shortly after re-homogenization (see below). In some cases, the H_2O content of unheated type-B MIs could also be estimated. The main solid phases in this inclusion type are muscovite (up to 50–60 vol%), topaz (~5 vol%) ± cryolite. In addition to alkali-chlorides (from 3.5 ± 0.3 up to 10 eq. wt% NaCl), the solutions contain boric acid up to 6 wt% (3.45 ± 1.1 wt%, mean for 20 MIs). In type-B MIs, the H_2O content is highly variable, from about 28–55 wt%. For this inclusion type, the high-frequency region of not homogenized MIs is characterized by the dominance of

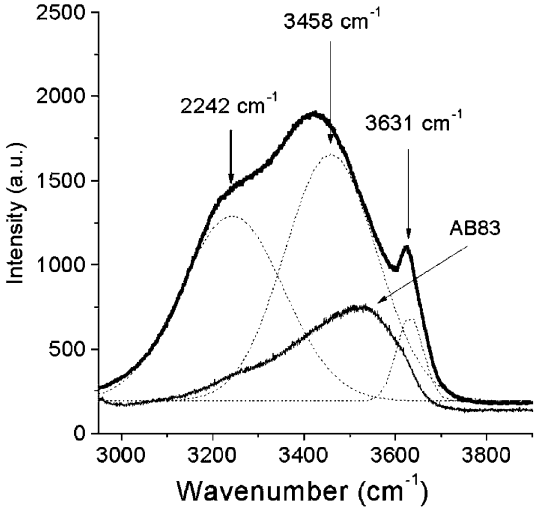

Fig. 3 The high-frequency region (3,000–3,800 cm^{-1}) of the unpolarized Raman spectrum of an unheated type-B MI. Gaussian deconvolution reveals that this broad asymmetric band is the result of three main bands at 3,242, 3,458, and 3,631 cm^{-1}. The two bands at 3,242 and 3,458 cm^{-1} reflect the dominance of molecular H_2O in the type-B inclusions. The relative sharp and symmetric band at 3,631 cm^{-1} can be traced back to OH-stretching vibrations of muscovite and topaz. AB83 is the reference spectrum of the albite glass with 11.71 wt% H_2O (see Thomas 2000). From the integral intensity ratio in the wave number range 3,000–3,800 cm^{-1} of the two spectra, an H_2O content in the type-B inclusion is ~42 wt%

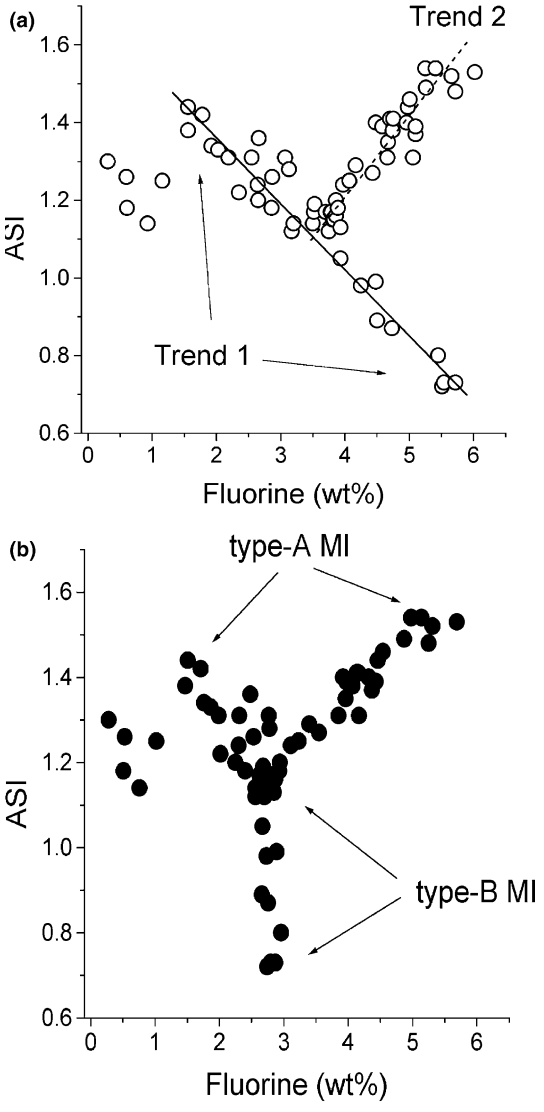

Fig. 4 Plot of the ASI versus the F content in the MIs. **a** ASI vs F of the water-free calculated analyses from Table 1. **b** ASI vs F for the same MIs, however H_2O is included

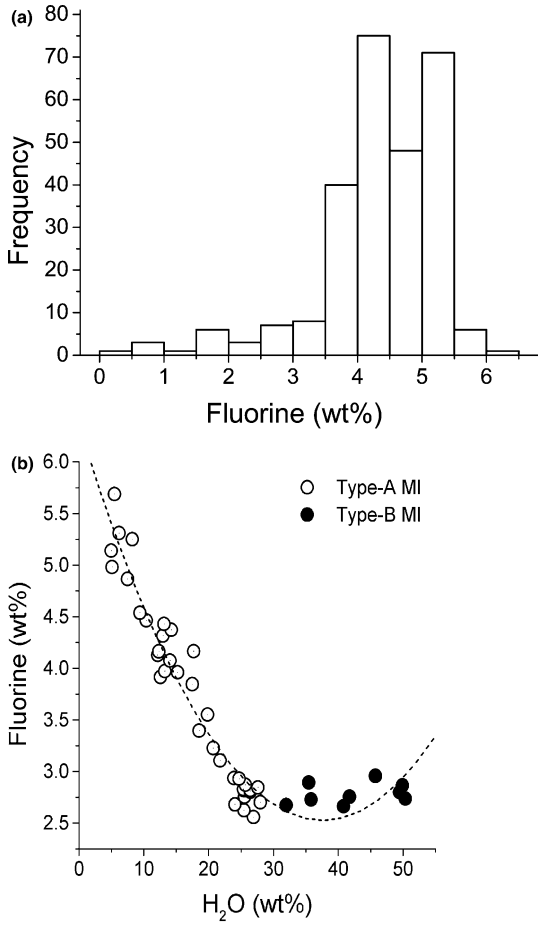

Fig. 5 **a** Frequency diagram of F in MIs, determined by microprobe analysis (270 microprobe analyses). **b** Plot of F vs. H_2O in MIs using the data given in Table 1, last column

molecular H_2O and a strong band at 3,625 cm^{-1}, which can be traced back to the high mica content (Fig. 3). The high F concentration of this inclusion type is indicated by topaz and cryolite daughter phases. The estimated bulk F concentration is ≥5 wt% (on an H_2O-free basis). These inclusions cannot be considered as "true" silicate MIs, because of the extreme H_2O concentrations. We can call this type "aluminosilicate-rich FI."

Electron-microprobe data for MIs re-homogenized mostly at ambient pressure (Table 1) indicate the heterogeneous composition of the trapped melts with respect to almost all elements monitored. Of the elements of most interest, the correlation patterns between the ASI and F were taken to group the MIs (Fig. 4a, b). Group I includes MIs, which display a negative correlation between ASI and F, following a trend hereafter indicated as *trend 1*. The second group involves inclusions, in which ASI and F is generally high and strongly positively correlated (*trend 2*). The five points (F <1.5 wt%, ASI $\sim$1.2) in Fig. 4a, b represent the bulk-rock composition. If we plot silicon versus fluorine, a quite analogous diagram results. A comprehensive discussion of the full data set in Table 1 will be the subject of a forthcoming paper.

Fluorine, chlorine, and water

In Fig. 5a is plotted the F concentration as a frequency histogram from 270 microprobe analyses of MIs. Fluo-

Table 2 Fluorine in the studied MIs

Group	Fluorine (wt%)	*n*
I	0.96 ± 0.50	5
II	2.01 ± 0.19	7
III	2.90 ± 0.28	16
IV	3.84 ± 0.12	42
V	4.31 ± 0.11	76
VI	4.94 ± 0.20	114
VII	5.64 ± 0.19	9

Concentrations: mean ± 1σ
n number of measurements

rine is generally enriched (up to 6 wt%), especially in type-A MIs, and shows (using single data points) seven concentration maxima (Table 2). The F concentration in the type-B MIs is more or less constant – it increases from about 2.5–3 wt% (under consideration of the H_2O content). Figure 5b shows the correlation of F vs H_2O in the MIs. This plot demonstrates that F is strongly enriched in the type-A MIs and decreases with rising water concentration in the MIs.

In most inclusions, the Cl concentration is low (≤ 0.05 wt%). However, a series of MIs has increasing Cl concentrations up to 0.4 wt% (Fig. 6), with the highest values in trend-2 MIs as defined in Fig. 4. Here, Cl increases proportionally with the F concentration (closed circles in Fig. 6). Because Cl partitions more strongly in favor of fluid relative to melt (Webster et al. 2004), there are two possibilities to produce such strong scatter shown in Fig. 6: (1) loss of Cl via fluid phase in the MIs during the homogenization procedure and (2) loss of Cl via fluid exsolution from the magma at fluid-saturated conditions. The mechanism for the two processes, however, is the same.

The minimum H_2O content was measured in large, isometric, crystalline MIs adopting the micro-thermometric/micro-volumetric technique outlined by Naumov (1979), which ignores the amount of H_2O present in H_2O-bearing minerals and glass remnants (see Thomas and Klemm 1997). This method suggests minimum H_2O concentrations of 6.3 ± 1.8 wt% (sample TH212) and 4.3 ± 0.2 wt% (sample 1159), respectively (analyses 1 and 2 in Table 3). Raman-spectroscopic determination of H_2O in glass in MIs re-homogenized at ambient

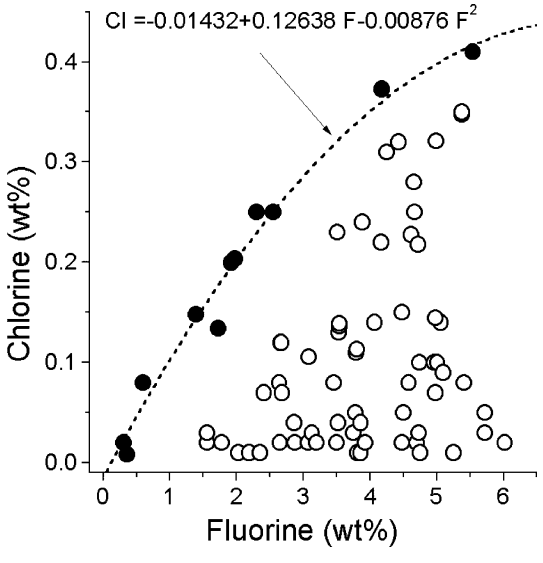

Fig. 6 Plot of the concentration (wt%) of Cl vs. F in homogenized MIs in quartz from Zinnwald granite sample TH212. The boundary curve (*dashed line*) can be regarded as a saturation curve for Cl in the Zinnwald melt as function of the F content. We interpret the *open circles* away from the *dashed line* as MIs, which have lost chlorine via fluid phase, mostly during the homogenization procedure or by loss of Cl via fluid exsolution from the magma at fluid-saturated conditions

pressure conditions was possible only in a small number of inclusions, in which the glassy portion did not fluoresce strongly (analyses 3–8 in Table 3). In most inclusions, the glass displays a strong fluorescence of unknown origin, which masks the O–H stretching vibration of hydroxyl groups in the high-frequency region. These inclusions are not suited for H_2O determination (Thomas 2000) with Raman spectroscopy. Re-homogenization at 850, 750, 700, 650, and 600°C at pressures of ~1,000 bar significantly reduced the intensity of fluorescence (see Table 3, No. 9-33). Type-B MIs usually contain higher, however variable H_2O concentrations between 28 and 55 wt%. In quartz of the 750°C experiment, we identified a great number of totally homogenized type-B MIs, with an average H_2O concentration of 28.6 ± 6 wt%. Immediately after quenching, some of these MIs were composed of a metastable homogeneous glass, which disintegrates after some hours into three phases: glass + liquid + vapor. This behavior can be traced back to the very low glass transition temperature (Tg) of such F- and H_2O-rich glass and the therewith associated strong change in the polymerization behavior (see Mysen et al. 2004).

Boron

Boron was measured in a selection of re-homogenized MIs only, primarily in those of group 2 (trend 2). In this inclusion group, the concentration is generally high and ranges from 0.7 to 2.6 wt% B_2O_3 (with an average of 2.2 wt%, see anal. #32 in Table 1). The three large type-A MIs shown in Fig. 1a contain an average of 2.4 ± 0.2 wt% B_2O_3 (in No. 32 of Table 1) and were probably trapped near the solvus crest (see below).

In the liquid H_2O phase of the H_2O-rich type-B MIs, re-homogenized at 750°C and 1,000 bar, large quantities of dihydroxyfluoroboric acid, $HBF_2(OH)_2$, were identified by Raman spectroscopy. This B–F complex is distinguished by a medium-strong Raman band at 871 cm^{-1} and a strong band at 731 cm^{-1} (e.g., Maya 1977). The band at 871 cm^{-1} is much wider than that of boric acid (H_3BO_3) in solution at 876 cm^{-1} (Fig. 7). Comparison of the intensity of the medium-strong 871 cm^{-1} band with that of a 1 wt% aqueous H_3BO_3 solution suggests a maximum $HBF_2(OH)_2$ of ~13.7 wt%. The 871 cm^{-1} band intensity was observed to decrease quickly during the measurement (450 mW for sample excitation), with only 2.6 and 1.3 wt% $HBF_2(OH)_2$ remaining after 600 and 3,000 s, respectively. Within the same time, the 876 cm^{-1} band intensity increases at the expense of the 871 cm^{-1} component. After 24-h, all bands in the 871–876 cm^{-1} region disappeared. Instead of these bands, a new band at 776 cm^{-1} appeared reflecting the formation of tetrafluoroborates of the composition MBF_4 (M = Li, Na, K, Rb, Cs). Formation of the 776 cm^{-1} band was accompanied with a strong widening and increase of the quartz bands at 795 and 806 cm^{-1}, which likely is related to

Table 3 Water content of MIs

No.	Group	Run-temperature (°C)	Inclusion diameter (μm)	Water content[a] (wt% ± 1σ)	Inclusion type	*n*
1	I	–	50	6.3 ± 1.8	A	2
2	I	–	33	4.3 ± 0.2	A	10
3	II	768	20	5.5 ± 0.5	A	9
4	II	768	20	9.2 ± 0.4	A	4
5	II	905	25	6.0 ± 0.5	A	6
6	II	905	15–25	16.1 ± 1.8	A	2
7	II	905	10–15	39.8 ± 4.0[b]	B	4
8	II	969	10–25	5.9 ± 0.8	A	8
9	III	750	8–18	2.7 ± 0.3	A	8
10	III	750	10–40	6.1 ± 1.1	A	13
11	III	750	30–50	9.9 ± 0.5	A	34
12	III	750	10–40	28.6 ± 6.0[b]	A/B	23
13	III	700	30	5.3 ± 0.7	A	12
14	III	700	15–40	7.1 ± 0.5	A	14
15	III	700	50–80	9.0 ± 0.6	A	46
16	III	700	10–70	12.6 ± 0.6	A	12
17	III	700	25	19.2 ± 1.7	A	6
18	III	700	20	35.0 ± 5.0[b]	B	3
19	III	650	20–50	7.1 ± 0.8	A	38
20	III	650	15	9.2 ± 0.5	A	5
21	III	650	10–20	14.0 ± 1.0	A	8
22	III	650	10–25	45.0 ± 6.0[b]	B	4
23	III	600	30	7.3 ± 0.2	A	6
24	III	600	10–20	51.0 ± 7.0[b]	B	4
25	IV	850	75	4.0 ± 0.6	A	23
26	IV	850	10–35	5.8 ± 1.0	A	19
27	IV	850	110–120	11.8 ± 1.3	A	17
28	IV	850	20–90	16.0 ± 0.6	A	12
29	IV	850	16	18.4	A	1
30	IV	850	18–30	3.5 ± 0.5	A	9
31	IV	850	20–35	6.6 ± 1.0	A	10
32	IV	850	75	9.9 ± 0.6	A	5
33	IV	850	25–84	16.0 ± 0.6	A	13
34	V	–	10–50	~42	B	5

[a]Mean of five to ten measurements on the inclusions
[b]Determined by Raman spectroscopy and volumetric measurements n number of studied MIs
Group I natural glass inclusion in quartz (not re-homogenized), very rare
Group II homogenized at ambient pressure, run time: 20 h
Group III cold-seal pressure vessel experiments, 750–600°C and 1,000 bar
Group IV hydrothermal rapid-quench experiment at 850°C and 1,000 bar
Group V natural type-B inclusion in quartz (not re-homogenized)

formation of metaboric acid (HBO_2), which has its strongest bands just in this region.

The observed, time-dependent behavior of these B species is in accordance with characteristics of aqueous solutions of fluoroborates during slow hydrolysis at room temperature (Gmelin 1926, 1954). In the case of dihydroxyfluoroboric acid, which is thermodynamically unstable, the relatively slow nucleation of HBO_2 crystals inhibits its dissociation (Maya 1977).

The high mobility of B is also reflected by the measured difference of boric acid in unheated and homogenized type-B MIs (750°C and 1,000 bar). Unheated inclusions contained an average of 3.45 ± 1.10 wt% H_3BO_3, whereas re-homogenized inclusions contained 0.7 ± 0.2 wt% H_3BO_3 only.

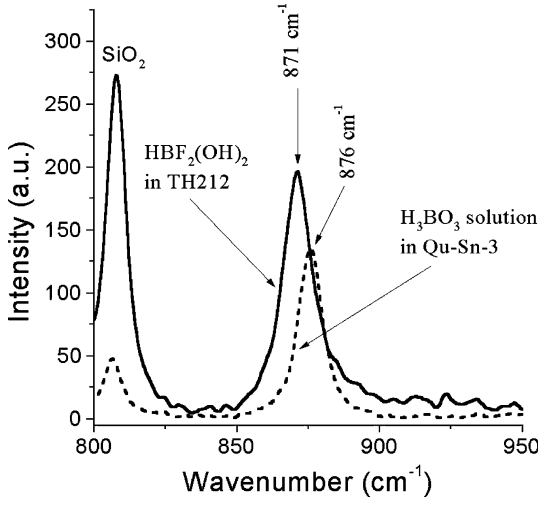

Fig. 7 Raman spectra of dihydroxyfluoroboric acid in a type-B MI, and of boric acid in an FI

Tin

The concentration of Sn in the type-A MIs, determined by EMP, ranges from 105 to 785 ppm, with an

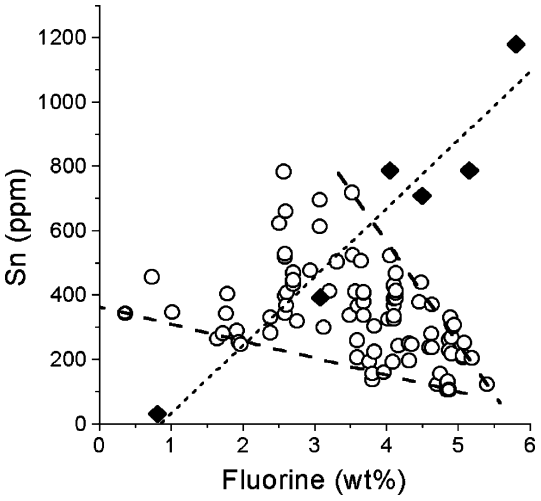

Fig. 8 Plot of Sn vs. F in the MIs. The *small dashed line* illustrates the evolution of the magmatic Sn concentration that has been established in MIs from Ehrenfriedersdorf in the western Erzgebirge (Thomas et al. 2003)

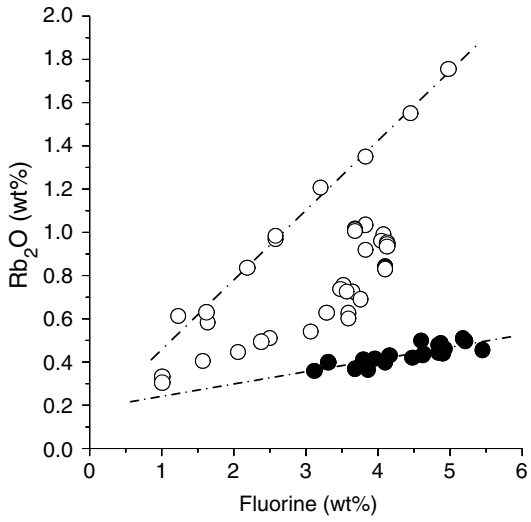

Fig. 9 Correlation of Rb_2O vs F in the MIs. See Fig. 3 for explanation of the *symbols*. The *half-filled symbols* display the melt evolution prior to significant Rb–Cs mica crystallization, which depleted the melt of some of Rb

average of 345 ppm ($n = 111$). The same, large scatter was observed also for other trace elements such as Cu (20-111 ppm, $n = 28$), Zn (100-1,360 ppm, $n = 31$), and Nb (112-910 ppm, $n = 19$). Synchrotron XRF measurements on two individual type-B MIs, which are the first ever, yield the following concentrations (in parts per million): Sn 510, Nb 680, and Mo 290. These inclusions contain also high Rb and Cs concentrations (in parts per million): Rb 5,300, Cs 2,900. On an H_2O-free basis we obtain (parts per million): Sn 850, Nb 1,130, Mo 485, Rb 8,830, and Cs 4,830, implying that these elements are also enriched in the type-B melt. Tin and F do not show a good correlation (Fig. 8).

Rubidium and cesium

The concentrations of Rb are generally high (> 0.4 wt% Rb_2O), but also scatter over a wide range (Fig. 9). The mean of 166 measurements is 0.67 ± 0.29 wt% Rb_2O. MIs following the peralkaline trend-1 show a weak increase of Rb with increasing F. In trend-2 MIs, Rb increases more strongly with F and appears to evolve along two pathways. The behavior of Cs resembles that of Rb. However, in contrast to Rb, the Cs content in the MIs is significantly lower (0.15 wt% Cs_2O, $n = 113$). The average Rb/Cs ratio is 4.5. The maximum measured concentrations of 2.1 wt% Rb_2O and 2.9 wt% Cs_2O yield an Rb/Cs ratio of 0.72, which may characterize the very end of magma evolution.

For the other important alkali element Li, only few SIMS data are available with a mean of 0.35 wt% Li_2O in type-A MIs. A discussion of the behavior of Li must be reserved for future studies.

Composition of fluid inclusions

Fluid inclusions in granite quartz

The FIs in quartz in granite are small (up to 25 μm in diameter) and are often composed of a concentrated NaCl + KCl (≥50 wt%) solution, a vapor bubble, and daughter minerals such as halite, sylvite, B-muscovite, nahcolite, calcite and others, showing that the primary magmatic fluids were concentrated aqueous solutions. However, the most frequent inclusions are two-phase aqueous inclusions which homogenize to the liquid phase or by critical phenomena at 396 ± 16°C and salinity of 3.2 ± 1.7 eq. wt% NaCl ($n = 250$) (see also Webster et al. 2004).

Secondary FIs, with low homogenization temperatures (100–200°C) and low salinity, display a mean concentration of about 0.29 ± 0.12 wt% H_3BO_3, showing the high mobility of B in the postmagmatic stage.

Fluid inclusions in hydrothermal quartz

Primary FIs in quartz intergrown with cassiterite from the main stage of SnO_2 deposition in the Zinnwald Sn–W deposit (e.g., Thomas 1982) were studied for the compositional relationship between late-stage melts and early, ore-forming hydrothermal solutions. The quartz sample contains large, up to 50 μm in diameter, primary FIs (Fig. 1d) arranged along growth zones. Secondary FIs are subordinate. The homogenization temperatures of the primary FIs in quartz and the surrounding cassiterite are nearly identical and amount to 390 ± 12°C ($n = 9$; Thomas 1982). Cryometric measurements, interpreted in light of the phase relations in the NaCl–KCl–H_2O ternary (Bodnar et al.1989), imply salt concentrations of 2.8 ± 0.2 wt% NaCl, and 7.9 ± 0.6 wt% KCl ($n = 6$).

Raman spectroscopy shows relatively high H_3BO_3 concentrations in the fluid: 0.92 ± 0.15 wt% ($n = 30$). One inclusion contains 5.1 ± 0.2 wt% H_3BO_3. The total volume ratio of topaz crystals, which are present in every FI, to the inclusion volume is directly proportional to the H_3BO_3 concentration, implying that the fluid contains constant proportions of B and F. One weight percent H_3BO_3 corresponds to a maximum F concentration (calculated as $NaBF_4$) of 2.2 wt% (e.g., Thomas 2002a). This F concentration is in excellent agreement with an F concentration of 2.1 ± 0.1 wt% obtained experimentally for fluids in equilibrium with the related F-rich melts from Zinnwald (Webster et al. 2004).

The fluid phase is enriched in various trace elements, which are also enriched in the melt fractions trapped as MI. Synchrotron XRF measurements on five individual FIs yield the following concentration averages (in parts per million): Fe 3,600, Cu 2,750, Zn 2,200, As 2,000, Cs and Sn 275, Cd and Sb 200, Rb 180, and Ag 100. The standard deviation is $\leq 20\%$ for each. The vapor phase is composed of H_2O, CO_2, CH_4, N_2 and H_2S [$X_{CO_2} = 0.744$; $X_{CH_4} = 0.198$; $X_{N_2} = 0.051$; $X_{H_2S} = 0.007$ on a H_2O - free basis].

In addition to this type of FI, another however rare primary FI group has been observed. The inclusions of this group are characterized by very high concentrations of $NaHCO_3$ (23.8 wt%) and slightly higher homogenization temperatures of 405 ± 2°C ($n = 15$). Synchrotron XRF measurements on five individual FIs of this group yield the following concentration averages (in parts per million): Fe ≤ 150, Cu 1,465, Zn ≤ 500, As 280, Rb 320, Sn 70, and Cs 220.

Fluid inclusions in cassiterite

Thermometric measurements on primary FIs in a large cassiterite crystal (5×5×2 cm) indicate a homogenization temperature of 431 ± 3.0°C ($n = 45$). These FIs homogenize in the liquid phase or with critical behavior. According to cryometric measurements on large inclusions (~50 µm in diameter), using the phase relations in the NaCl-KCl-H_2O ternary (Bodnar et al. 1989), salt concentrations of 4.9 wt% NaCl and 6.7 wt% KCl ($n = 6$) were determined, corresponding to an NaCl/KCl ratio of about 0.5. The boric acid concentration of 11 primary FIs was 2.6 ± 0.5 wt%. The vapor phase consisted of H_2O, CO_2, CH_4, and N_2[$X_{CO_2} = 0.672$; $X_{CH_4} = 0.208$; $X_{N_2} = 0.119$ on a H_2O - free basis].

In daughter-crystal rich FIs (which homogenize to the liquid phase at 510 ± 4°C, $n = 10$) in cassiterite from the Sn deposit Krupka, Czech Republic (6.2 km SE of Zinnwald), villiaumite (NaF) daughter crystals were identified. From the dissolution temperature of NaF (104°C), an NaF concentration of 4.85 wt% (equivalent to 2.2 wt% F) was estimated according to Nývlt (1977). This is a minimum F concentration, however, because another F phase (about 5–10 vol%) is present in these inclusions. Very strong Raman bands at 185, 198, 385, and 3,446 cm^{-1} suggest this phase is a metal (II) hexafluorosilicate (IV) salt (see Jenkins and Lewis 1981).

Discussion

Water concentrations

In Table 3 are given the results of the H_2O determination, obtained mostly by using the Raman-spectroscopic technique or from a combination of Raman spectroscopy and volumetric estimations. The results vary very strongly (from 2.7 to 55 wt%). At first sight, one does not recognize any relationships. This is true for all studied MI of the groups I, II, IV, and V. If we plot, however, the H_2O concentration versus the experimental homogenization temperature of group III MIs, then we obtain from the bulk H_2O concentration (using the highest H_2O concentrations of the type-A MIs) of both MI types a X_{H_2O} -T pseudobinary diagram (Fig. 10). From this diagram it can be seen that the H_2O concentration in the type-A MI tends to increase continuously from 7.3 to 28.6 wt% with increasing homogenization temperatures from 600 to 720°C. Concentrations of H_2O in the coexisting type-B MI decrease from 51 to 28.6 wt% over the same temperature range. The solvus crest is located at 720°C and 28.6 wt% H_2O (see Thomas et al. 2000). The temperature of 720°C was chosen from symmetry reasons and from the determined minimum trapping temperature (see chapter 2.2). This solvus was used to estimate the H_2O content for the MIs presented in Table 1 (last column).

At the low lithostatic pressure of the shallowly emplaced granites of Zinnwald (~1,000 bar; Thomas and Klemm 1997; Stemprok et al. 2003), the dissolution of 6 to 28 wt% of H_2O in melt requires the presence of F and

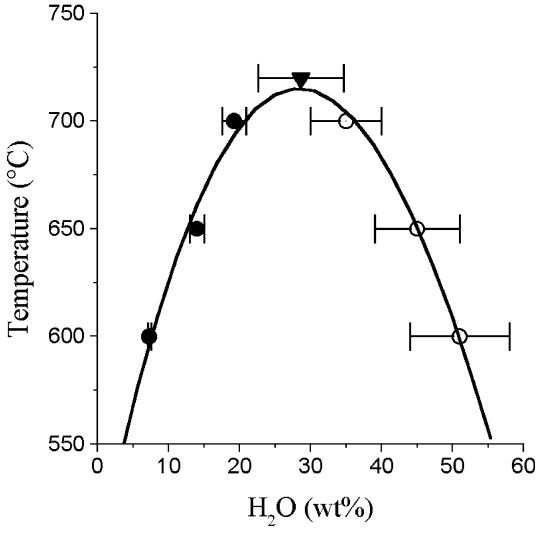

Fig. 10 Pseudobinary X_{H2O} vs T plot of re-homogenized type-A (*closed circles*) and type-B MI (*open circles*) in granite quartz from Zinnwald. The solvus crest is indicated by the *inverted triangle*

other fluxing volatiles in extraordinarily high amounts as observed here and in the companion paper of Webster et al. (2004). The originally homogeneous melt unmixes into two phases, a "normal," H_2O-rich melt (type-A) and a highly mobile, extremely H_2O-rich melt (type-B) or an aluminosilicate-rich fluid. This can be seen by the coexistence of these MIs that were re-homogenized between 600 and 750°C and 1,000 bar in the quartz phenocrysts. In addition to totally homogenized MIs, type-B MIs composed of a silicate glass + water + vapor contain a bulk H_2O concentration of 28.6 ± 6 wt%. These MIs are interpreted to represent the originally homogeneous melt that underwent unmixing during or immediately after quenching (see Thomas et al. 2003). The two types of MIs also coexist with vapor-rich FIs.

The appearance of two chemically distinct FIs can be explained by the fact that both coexisting melts can also separate different fluid phases of contrasting composition. The type-A melts separate acidic fluids, with boric acid and B–F-complexes, and the type-B melts separate more basic fluids, with nahcolite as an example. These contrasting fluids were observed in numerous pegmatites and granites worldwide (unpublished results for Ehrenfriedersdorf, Pechtelsgrün, Germany; Bornholm island, Denmark; Orlovka, Russia; Tanco, Canada). These fluids were instrumental in the extreme hydrothermal alteration observed in the mineralized rocks. The appearance of different inclusion types, often in the same growth zone, aggravates the study and interpretation of melt and FIs (cp. Kamenetsky et al. 2002, 2004).

Chlorine concentration

Another volatile element that in part shows significantly higher concentrations than those determined by Webster et al. (2004), is Cl. Chlorine is doubtless concentrated in the separate fluid phase inside unheated MIs, which usually is lost during high-T heating at ambient pressure by decrepitation or leakage. Cryometric measurements indicate NaCl-equivalent concentrations of 5–10 wt%, which are equivalent to 1,200–2,500 ppm Cl in the melt. Another possibility is the loss of Cl via fluid exsolution from the magma at fluid-saturated conditions (Fig. 6). The exsolution of halogen-charged fluids from the F-enriched Zinnwald granitic magma modified the Cl, alkali, and F content of the residual melt. The exsolution of Cl and F is discussed in detail by Webster et al. (2004).

Fluorine concentration

From the data in Table 1 it is obvious that a strong enrichment of F during magma evolution is characteristic of the strongly differentiated topaz–albite–zinnwaldite granites from Zinnwald and elsewhere (e.g., Webster et al. 2004; Dolejš and Baker 2004). The high F content in the melt is reflected also in the primary mineral paragenesis of the granite rocks, which is now preserved only in the quartz phenocrysts. The coexistence of quartz, albite, orthoclase, topaz, fluorite, and cryolite in the Zinnwald topaz–albite granite at about 600°C and 1,000 bar (near solidus conditions) defines, according to Dolejš and Baker (2004), a very high F activity $\mu(F_2O_{-1}) = -460$ kJ at $\mu(Na_2O) = -773$ kJ in the melt and a log $a(HF^0) = -0.4$ in the coexisting fluid. Topaz and cryolite daughter phases, together with the very strong Raman band at 3,631 cm^{-1} (Fig. 3), show that the F concentration in the type-B MIs is also high (~3 wt%). The F distribution between type-A and type-B melt at 600°C is about 1.9, demonstrating that F is enriched in favor of the peraluminous melt (see Fig. 5b). At the critical point (see Fig. 10), the distribution coefficient is equal to 1. It is important to underline the fact that F and H_2O in combination will be even more effective in reducing melt viscosities than these components alone (Dingwell 1987). In aluminosilicate melts, dissolved F breaks bridging oxygen bonds, causes depolymerization, and decreases viscosity (Mysen et al. 2004). The high-temperature magmatic fluids are rich in F as well, as indicated by daughter crystals of topaz in FIs in hydrothermal quartz and villiaumite and hexafluorosilicate (IV) salts in FIs in cassiterite.

Interpretation of the melt-evolution trends

The data points representing the bulk rock plot outside the evolution trend for the MIs (Fig. 4a). This can be explained by loss of F and Al during the postmagmatic high-temperature stage.

For the MIs, the relationships not only between ASI and F, but also between other elements (e.g., Si), highlight an evolution of late-stage melts along two major compositional pathways. Trend 1, reflecting a decrease in ASI with increasing F (Fig. 4a), is in accord with the alkaline fractionation trend in B–P–F-rich granitic melts: the melts become increasingly alkaline, silica-poor, and sodic as the cognate crystallizing rock composition becomes increasingly silicic, aluminous, and potassic (D. London, personal communication). A roughly negative correlation between ASI and F, and an increase of F and alkaline elements with decreasing temperature, was also the outcome of an experimental study of a B–P–F-rich synthetic granite pegmatite at 0.1 and 0.2 GPa (Veksler and Thomas 2002). Furthermore, in silica-saturated compositions, the crystallization of quartz and feldspars will further increase the peralkalinity of the melt as the temperature decreases. With increasing peralkalinity the solubility of H_2O also increases. Therefore, it seems appropriate to suggest that trend 1 corresponds to melt evolution triggered by fractional crystallization. This interpretation also holds for the elemental abundances of Rb and Cl shown as filled symbols in the Figs. 6 and 9. During this process, F and H_2O accumulate strongly in the silicate melt up to about 3.5 and 28 wt%, respectively. The originally homogeneous melt

separates at this point into two phases with strongly different character (see Fig. 10). In this light, the interpretation of the peraluminous MIs (trend 2) showing the strong enrichment of several components is very simple. If this trend is not an analytical artifact of accidentally trapped minerals in the quartz host (for which no evidence exists), two hypotheses remain. One hypothesis involves the late-stage separation of a new, peraluminous melt phase from that melt, which originally evolved along the trend 1 line (e.g., Fig. 4). From the data in Figs. 4 and 10 it can be easily established that the homogeneous system becomes unstable at about 3.5 wt% F and 28.6 wt% H_2O by liquid–liquid immiscibility.

The second potential explanation involves the so-called BL effect, when during rapid growth of crystals from a viscous granite melt, a flux-enriched BL melt may form in advance of the crystal front (e.g., London 1992, 1999; Anderson 2003; Lowenstern 2003). The melt in the BL is depleted in components compatible with the host phase and enriched in components that are incompatible with the host, i.e., it represents an accumulation of elements that would be enriched at the end of magma differentiation (Smith et al. 1955).

The dimension of the BL depends on melt viscosity and mineral growth conditions. It may be ~10–15 μm for basalts and 100–150 μm for some rhyolitic melts (Pletchov and Trusov 2000). However, this width of the BL refers to a common, relatively dry rhyolitic melt, which has a viscosity of about 10^5 Pa s at 700°C (Baker and Vaillancourt 1995). A viscosity less than about 10^2 Pa s is necessary that an acid melt is able to move with respect to their matrix (McKenzie 1985). This viscosity is significantly higher than the viscosity of the most evolved, F–H_2O-rich melt, that is about 1 Pa s or lesser (at 700°C) using the empirical method of Shaw (1972), or the results represented by Audétat and Keppler (2004). At this low viscosity, the thickness of the BL should be <10 μm (Pletchov and Trusov 2000). This dimension is smaller than the diameter of most of the studied MIs. Moreover, Lu et al. (1995), Webster and Duffield (1994), Webster and Rebbert (2001), and Webster et al. (2003) have specifically addressed the issue of BL and found no evidence to support its importance. Finally, Wallace et al. (1999) concluded that MIs greater than 50 μm could not be affected by the BL in the Bishop Tuff, California.

Anyway, the BL problem is only poorly understood and any inference on its significance remains speculative, particularly because the thickness of the BL will vary dramatically with melt composition, pressure, temperature, and rate of crystallization. At this time, we are unable to systematically and rigorously treat, model or predict the presence of and the consequences of BL melts along the surfaces of growing quartz phenocrysts in the late-stage melts like those at Zinnwald. Almost nothing is known about the identity of trace element complexes in the melts, which precludes any serious quantitative estimate of the BL effect.

The very strong enrichment of some elements in the studied MIs can be alternatively and simply explained by "normal" fractional-crystallization differentiation and liquid immiscibility. Audétat and Pettke (2003) have shown that the Cs content of MIs can be used to estimate the melt crystallinity at the time of their entrapment. If we take the fraction of the melt as an equivalent to its crystallinity, and plot the Cs concentrations given in Table 4 (starting with 50 ppm for the least-differentiated granites of the region) against the melt-fraction, linear trends are obtained by least-square fits (Fig. 11). Similar plots for F, H_2O, and Rb result in roughly the same melt fractionations (MF) as in the Cs plot. The sub-parallel fractionation curves for F and H_2O are an expression of the close correlation of the two species. Because of the stronger incompatibility of Cs than Rb, the slope in the Cs plot rises steeply.

The strongest enrichment in H_2O, F, Cs, Rb and other elements is approached in melt fractions that represent about 1/100 of the original melt volume. At first glance, this fraction seems negligibly small. However, if the initial melt volume was 660 km^3 (see Tischendorf 1988) with 50 ppm Cs, then 0.2 vol% melt corresponds to a volume of about 1.32 km^3 with 1,700 ppm Cs, equivalent to about 5.6 million metric tons of Cs. Similar results are obtained for Sn using a four-step process of partial melting and differentiation assuming equilibrium conditions (Tischendorf 1988).

Enrichment of ore-forming elements

By the very low viscosity and favorable wetting angle, the extremely H_2O- and F-rich melts or silicate-rich solutions are excellent extraction media for all elements, which are concentrated at the grain boundaries, because

Table 4 Data set for the construction of the fractionation curves for Cs, Rb, F and H_2O

Melt fraction (%)	Cs (ppm)	Rb (ppm)	F (wt%)	H_2O (wt%)
100	50	3,795	0.93	3.3
7	212		2.03	6.6
1	660		3.17	10.6
0.2	1,700		5.25	16.2
0.07	3,820		6.44	21.6
0.006	13,535		11.66	42
40.30		5,596	1.23	
14.02		5,752	1.62	
13.4		5,331	1.6,4	
4.4		7,635	2.19	
2.4		8,980	2.58	
1.03		11,028	3.20	
0.52		12,345	3.83	
0.29		14,173	4.45	
0.19		16,048	4.98	
0.18		16,368	5.06	

The melt fraction numbers (MFNs) were calculated using Cs (50 ppm as the starting point and 27,070 ppm as the ending point, corresponding to MFNs of 100 and 0.001%, respectively).
Data from Tables 1, 3 and Fig. 5

they cannot be inserted into the crystal lattice of quartz and feldspar. By the high mobility and solution capacity of such a "fluid," this percolating solution collects everything available on its way through the crystallizing granite (see Audétat and Keppler 2004; Keppler 2004; Sirbescu and Nabelek 2003a and b). It enhances the element diffusivities, permitting uncommonly strong enrichment of many trace elements and their later extraction by fluids exsolved from the melt. Melts of such a low viscosity can form an interconnected network and can move over large distances from the source (Thomas et al. 2000, 2003), allowing ore components to accumulate at the top of a cupola prior to completion of magmatic crystallization (see also Lowenstern 1994).

Webster et al. (2004) have shown experimentally that at high F concentrations in the melt, the distribution of F, and potentially that of Sn, between fluid and melt are greater than expected for F-poor melts. The F concentration in the ore-bearing fluid at Zinnwald is similar or even greater than the Cl concentration (Webster et al. 2004). Thus, compared to the situation at Zinnwald, results of previous experimental work revealing the preferential distribution of F into the granitic melt, and of Cl into the residual granitic fluid, do not hold universally true (e.g., Jackson and Helgeson 1985; Keppler and Wyllie 1991). In analogy to Audétat and Pettke (2003), our results suggest that the melt attained fluid saturation early in the evolution and that in all stages, a B-, F- and Cl-rich fluid coexisted with the volatile-rich melts. As shown for the type-B MIs, B and F form complexes as dihydroxy-fluoroboric acid $HBF_2(OH)_2$ or its derivatives at room temperature. We assume that similar or related complexes may be stable at elevated temperatures and pressures in magmas like these, probably allowing more efficient extraction of F from the melt into the fluid as is suggested from previous investigations of B-free systems. During further cooling, $HBF_2(OH)_2$ became unstable; B formed the very stable boric acid (H_3BO_3) and F reacted with aluminum forming hydrothermal topaz. Fluoroboric acid and its hydroxy derivatives are excellent solvents for some metal oxides (Gmelin 1954; Saavedra et al. 1974). This would provide an effective mechanism for the dissolution of Sn into the fluid phase. Tin may be transported as Sn tetrafluoroborate [$Sn(BF_4)_2$], which at room temperature, is a colorless liquid with a low boiling point (~100°C), is completely soluble in H_2O, and reacts strongly acidic.

Other evidence for the presence of F–B-rich supercritical fluids during formation of the eastern Erzgebirge Sn province comes from MIs in quartz of the pyknite rock (composed of topaz, quartz, and zinnwaldite) from Altenberg in the immediate neighborhood of Zinnwald (see Table 1). Altenberg is the largest Sn deposit in central Europe (Baumann et al. 2000). Here, an F-rich supercritical fluid, or highly mobile melt, transformed the primary mineral phases orthoclase and biotite of a stockscheider pegmatite into pyknite. The transforming

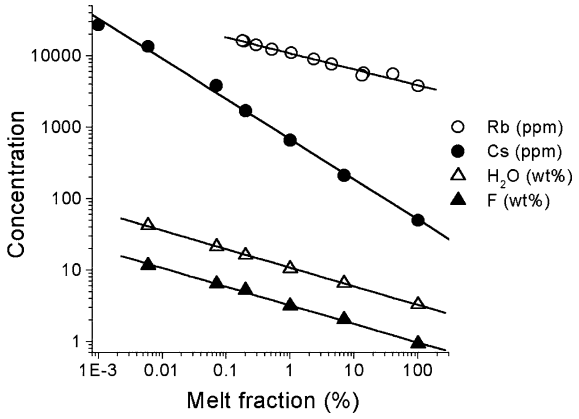

Fig. 11 Fractionation curves of Cs, Rb, F, and H_2O (concentration vs crystallinity) calculated from selected concentrations given in Tables 1, 2 and Fig. 5 (peraluminous trend). The used data are presented in Table 3. Please note the same abscissa distances for Cs, F, and H_2O

fluid (trapped now as type-B MIs) is characterized by a B_2O_3 concentration of about 1 wt%, corresponding to about 1.8 wt% H_3BO_3. The high F activity of this fluid is also indicated by the daughter-crystal phases (malladrite [Na_2SiF_6] and hieratite [K_2SiF_6]) in the high-temperature (520 ± 60°C) FIs in topaz and quartz (see Thomas 1982).

Extraction of Sn started early in the history, with the onset of the volatile saturation at about 3.5 wt% F according to Fig. 4 and ended with the final solidification of the magmas, giving rise to the surprisingly low Sn contents measured in most of the F-rich MIs from Zinnwald (e.g., Fig. 8). The Sn–F pattern supports the conclusions of Webster et al. (2004) that a large portion of the primary Sn concentrations in the melt has been extracted into fluids before MI entrapment was finished. Initial Sn concentrations in the melt may approximate the highest value (800 ppm) shown in Fig. 8, which approximates the values measured in MIs from the Sn granite–pegmatite system at Ehrenfriedersdorf in the western Erzgebirge (Webster et al. 1997; Thomas et al. 2003). Obviously, as shown by the first synchrotron XRF measurements, some Sn is also enriched in the type-B melt (850 ppm on H_2O-free basis).

The relatively low average Sn concentration of 275 ppm in the FIs in quartz from the quartz–cassiterite ore sample from this study can be attributed to co-precipitation of both minerals. During deposition of cassiterite, most of the Sn was sequestered from the fluid phase trapped in the host quartz.

The Rb/Cs ratio is a strong fingerprint for the close genetic relations between melts and fluids at Zinnwald. In the least evolved melt fractions trapped as MIs, the Rb/Cs ratio is already low, but consistently >4.5. The Rb/Cs ratio of the most evolved melts averages to 0.62 (see Table 1, column 12 and 13) and equals that measured in the FIs (0.6 on average). Hydrothermal brines from Ehrenfriedersdorf trapped as FIs, which contain

large daughter crystals of halite, montebrasite, sphalerite and other minerals, have a similar Rb/Cs ratio of 0.43 ± 0.06 (Rickers et al. 2004).

Concluding remarks

The results from this study complement experiments of Webster et al. (2004) and add important information on melt evolution by utilizing melt-inclusion reheating procedures. With a combination of appropriate experimental and analytical methods, the most optimal results were achieved. These include (a) re-homogenization of crystalline MIs with ambient and high-pressure, rapid-quench experiments, (b) determination of H_2O in re-homogenized MIs by Raman spectroscopy, (c) EMP and SIMS analysis of major, minor, and trace elements in H_2O-rich glasses, (d) determination of B with the EMP and, in part, with Raman spectroscopy, (e) non-destructive analysis of trace elements in FIs and MIs with synchrotron radiation induced XRF using Monte Carlo simulations for quantification, and (f) HDAC experiments for the study of the phase behavior of type-B MI during heating and cooling. The complexity of processes associated with the evolution of highly evolved silicate liquids requires a study of a large number of MIs and FIs in carefully selected samples.

In corroboration with earlier results (Thomas et al. 2000, 2003), this study provides additional evidence for the combined control of H_2O, B, and F on late-stage melt evolution and for the extraction and transport of Sn in the Erzgebirge metallogenetic province and similar Sn-bearing, magmatic-hydrothermal systems elsewhere. Furthermore, these results provide new evidence for silicate-melt immiscibility and the existence of supercritical, silicate-rich fluids at low pressure. The proof of low-viscosity, highly mobile aluminosilicate melts and silicate-rich fluids at low temperatures is important not only for better understanding pegmatite-forming processes, but also for improving our knowledge on the evolution of highly evolved, mineralized granite-forming melts.

Acknowledgements D. Rhede and Mrs. O. Appelt are thanked for their help with EMP analysis, and G. Berger for preparation of the extensive suite of samples. We are grateful to the Hamburger Synchrotronstrahlungslabor HASYLAB at the Deutsches Elektronen-Synchrotron (DESY), Hamburg, for beamtime at beamline L. I. Veksler, R. Schulz, and Mrs. H. Steigert assisted us at several high-pressure re-homogenization experiments. We thank Ilya Veksler for preparing the dry PR-glass used for HDAC experiments. In addition, we wish to express our appreciation to C. Schmidt and I. Veksler for performing some HDAC experiments. The work benefitted from stimulating discussions with A. Anderson, W. Heinrich, D. London, I. Veksler, and H. Beurlen. The study was supported by the Deutsche Forschungsgemeinschaft (DFG) through the grant Th 489 to R. Thomas, and was in part conducted within the framework of the DFG Priority Program SPP 1055 "Bildung, Transport und Differenzierung von Silikatschmelzen". Constructive reviews and helpful comments by D. Kamenetsky and P. Nabelek are gratefully acknowledged.

References

Anderson AT (2003) An introduction to melt (glass + crystals) inclusions. In: Samson I, Anderson A, Marshall D (eds) Fluid inclusions—analysis and interpretation, short course series (Raeside R series ed), chap 14, vol 32. Vancouver, British Columbia, pp 353–364

Audétat A, Keppler H (2004) Viscosity of fluids in subduction zones. Science 303:513–516

Audétat A, Pettke T (2003) The magmatic-hydrothermal evolution of two barren granites: a melt and fluid inclusion study of the Rito del Medio and Cañada Pinabete plutons in northern New Mexico (USA). Geochim Cosmochim Acta 67:97–121

Baker DR, Vaillancourt J (1995) The viscosity of $F + H_2O$-bearing granitic melts and implications for melt extraction and transport. Earth Planet Sci Lett 132:199–211

Bassett WA, Shen AH, Bucknum M, Chou I-M (1993) A new diamond anvil cell for hydrothermal studies to 2.5 GPa and from −190 to 1200°C. Rev Sci Instrum 64:2340–2345

Baumann L, Kuschka E, Seifert T (2000) Lagerstätten des Erzgebirges. Enke in Georg Thieme Verlag Stuttgart, p 300

Bilderback DH, Huang R (2001) X-ray tests of microfocusing mono-capillary optic for protein crystallography, nuclear instruments and methods in physics research, Section A: accelerators, spectrometers, detectors and associated equipment, vol 467–468, part 2, pp 970–973

Bodnar RJ, Sterner SM, Hall DL (1989) Salty: a Fortran program to calculate compositions of fluid inclusions in the system NaCl–KCl–H_2O. Comput Geosci 15:19–41

Chabiron A, Pironon J, Massare D (2003) Characterization of water in synthetic rhyolitic glasses and natural melt inclusions by Raman spectroscopy. Contrib Miner Petrol 146:485–492

Danyushevsky LV, McNeill AW, Sobolev AV (2002) Experimental and petrological studies of melt inclusions in phenocrysts from mantle-derived magmas: an overview of techniques, advantages and complications. Chem Geol 183:5–24

Devine JD, Gardner JE, Brack HP, Layne GD, Rutherford MJ (1995) Comparison of microanalytical methods for estimating H_2O contents of silicic volcanic glasses. Am Miner 80:319–328

Dingwell DB (1987) Melt viscosities in the system $NaAlSi_3O_8$–H_2O–F_2O_{-1}. In: Mysen BO (ed) Magmatic processes: physicochemical principles. The Geochemical Society, Special Publication No. 1, pp 423–431

Dolejš D, Baker DR (2004) Thermodynamic analysis of the system Na_2O–K_2O–CaO–Al_2O_3–SiO_2–H_2O–F_2O_{-1}: stability of fluorine-bearing minerals in felsic igneous suites. Contrib Miner Petrol 146:762–778

Falkenberg G, Rickers K, Bilderback DH, Huang R (2003) A single-bounce capillary for focusing of hard X-rays. HASYLAB Annual report 2003, pp 71–74

Fuhrman ML, Lindsley DL (1988) Ternary-feldspar modeling and thermometry. Am Miner 73:201–215

Gmelin L (1926) Gmelins Handbuch der anorganischen Chemie, System-Nr. 13 Bor, 8. Auflage, Verlag Chemie GmbH., Leipzig-Berlin, p 142

Gmelin L (1954) Gmelins Handbuch der anorganischen Chemie, System-Nr. 13 Bor, Ergänzungsband, Verlag Chemie GmbH., Weinheim/Bergstrasse, p 253

Goldstein RH, Reynolds TJ (1994) Systematics of fluid inclusions in diagenetic minerals. Society for Sedimentary Geology Short Course 31, p 199

Jackson KJ, Helgeson HC (1985) Chemical and thermodynamic constraints on the hydrothermal transport and deposition of Sn: I. Calculation of the solubility of cassiterite at high pressure and temperature. Geochim Cosmochim Acta 49:1–22

Jenkins TE, Lewis J (1981) A Raman investigation of some metal (II) hexafluorosilicate (IV) and hexafluorotitanate (IV) salts. Spectrochim Acta 37A:47–50

Kamenetsky VS, van Achterbergh E, Ryan CG, Naumov VB, Mernagh TP, Davidson P (2002) Extreme chemical heterogeneity

of granite-derived hydrothermal fluids: an example from inclusions in a single crystal of miarolitic quartz. Geology 30:459–462
Kamenetsky VS, Naumov VB, Davidson P, van Achterbergh E, Ryan CG (2004) Immiscibility between silicate magmas and aqueous fluids: a melt inclusion pursuit into the magmatic-hydrothermal transition in the Omsukchan Granite (NE Russia). Chem Geol 210:73–90
Keppler H (2004) The properties of subduction zone fluids. EMPG-X Symposium Abstracts/Lithos 73:S56
Keppler H, Wyllie PJ (1991) Partitioning of Cu, Sn, Mo, W, U, and Th between melt and aqueous fluid in the systems haplogranite–H_2O–HCl and haplogranite–H_2O–HF. Contrib Miner Petrol 109:139–150
London D (1992) The application of experimental petrology to the genesis and crystallization of granitic pegmatites. Can Miner 51:403–420
London D (1999) Melt boundary layers and the growth of pegmatite textures. Can Miner (abstr) 37:826–827
Lowenstern JB (1994) Dissolved volatile concentrations in an ore-forming magma. Geology 22:893–896
Lowenstern JB (2003) Melt inclusions come of age: volatiles, volcanoes, and Sorby's legacy. In: De Vivo B, Bodnar RJ (eds) Melt inclusions in volcanic systems – methods, applications and problems. Elsevier, Amsterdam, pp 1–21
Lu F, Anderson Jr AT, Davis AM (1995) Diffusional gradients at the crystal/melt interface and their effect on the composition of melt inclusions. J Geol 103:591–597
Massare D, Métrich N, Clocchiatti R (2002) High-temperature experiments on silicate melt inclusions in olivine at 1 atm: inference on temperatures of homogenization and H_2O concentrations. Chem Geol 183:87–98
Maya L (1977) Fluoroboric acid and its hydroxy derivatives – solubility and spectroscopy. J Inorg Nucl Chem 39:225–231
McGee JJ, Slack JF, Herrington JR (1991) Boron analysis by electron microprobe using MoB_4C layered synthetic crystals. Am Miner 76:681–684
McKenzie D (1985) The extraction of magma from the crust and mantle. Earth Planet Sci Lett 74:81–91
Morgan VI GB, London D (1996) Optimizing the electron microprobe analysis of hydrous alkali aluminosilicate glasses. Am Miner 81:1176–1185
Mysen BO, Cody GD, Smith A (2004) Solubility mechanism of fluorine in peralkaline and meta-aluminous silicate glasses and in melts to magmatic temperatures. Geochim Cosmochim Acta 68:2745–2769
Naumov VB (1979) Determination of concentration and pressure of volatiles in magmas from inclusions in minerals. Geochem Int 16:33–40
Nývlt J (1977) Solid–liquid phase equilibria. Elsevier, Amsterdam, p 248
Pletchov PY, Trusov SV (2000) The influence of boundary layer effects on the melt inclusions compositions. Exp Geosci 9:39–41
Rickers K, Thomas R, Heinrich W (2004) Trace-element analysis of individual synthetic and natural fluid inclusions with synchrotron radiation XRF using Monte Carlo simulations for quantification. Eur J Miner 16:23–35
Roedder E (1984) Fluid inclusions. In: Reviews in mineralogy, vol 12, p 644
Roedder E (2003) Significance of melt inclusions. In: De Vivo B, Bodnar RJ (eds) Melt inclusions in volcanic systems – methods, applications and problems. Elsevier, pp 15–16
Saavedra J, Sanchez AG, Perez SR (1974) Decomposition and analysis by atomic absorption photo-spectrometry of silicate rocks. Chem Geol 13:135–139
Shaw HR (1972) Viscosities of magmatic silicate liquids: an empirical method of prediction. Am J Sci 272:870–893
Sirbescu M-LC, Nabelek PI (2003a) Crustal melts below 400°C. Geology 31:685–688
Sirbescu M-LC, Nabelek PI (2003b) Crystallization conditions and evolution of magmatic fluids in the Harney Peak Granite and associated pegmatites, Black Hills, South Dakota – evidence from fluid inclusions. Geochim Cosmochim Acta 67:2443–2465
Smith VG, Tiller WA, Rutter JW (1955) A mathematical analysis of solute redistribution during solidification. Can J Phys 33:723–745
Stemprok M, Holub FV, Novák JK (2003) Multiple magmatic pulses of the Eastern Volcano-Plutonic Complex, Krušné hory/Erzgebirge batholith, and their phosphorus contents. Bull Geosci 78:277–296
Student JJ (2002) Silicate melt inclusions in igneous petrogenesis. PhD Dissertation, Virginia Tech. http://scholar.lib.vt.edu/theses/available/etd-08192002-150340/
Student JJ, Bodnar RJ (1999) Synthetic fluid inclusions XIV: microthermometric and compositional analysis of coexisting silicate melt and aqueous fluid inclusions trapped in haplogranite–H_2O–NaCl–KCl system at 800°C and 2000 bars. J Petrol 40:1509–1525
Tabaksblat R, Meier RJ, Kip BJ (1992) Confocal Raman microspectroscopy: theory and application to thin polymer samples. Appl Spectrosc 46:60–68
Thomas R (1982) Ergebnisse der thermobarogeochemischen Untersuchungen an Flüssigkeitseinschlüssen in Mineralen der postmagmatischen Zinn-Wolfram-Mineralisation des Erzgebirges. FFH C 370, p 85 + 15
Thomas R (1989) Untersuchungen von Schmelzeinschlüssen und ihre Anwendung zur Lösung lagerstättengeologischer und petrologischer Problemstellungen. Dissertation B, Bergakademie Freiberg, p 131
Thomas R (1994a) Estimation of the viscosity and the water content of silicate melts from melt inclusion data. Eur J Miner 6:511–535
Thomas R (1994b) Fluid evolution in relation to the emplacement of the Variscan granites in the Erzgebirge region: a review of the melt and fluid inclusion evidence. In: Seltmann, Kämpf, Möller (eds) Metallogeny of collisional orogens. Czech Geological Survey, Prague, pp 70–81
Thomas R (2000) Determination of water contents of granite melt inclusions by confocal laser Raman microprobe spectroscopy. Am Miner 85:868–872
Thomas R (2002a) Determination of the H_3BO_3 concentration in fluid and melt inclusions in granite pegmatites by laser Raman microprobe spectroscopy. Am Miner 87:56–68
Thomas R (2002b) Determination of water contents in melt inclusions by laser Raman spectroscopy. In: De Vivo B, Bodnar RJ (eds) Proceedings of the workshop – short course on volcanic systems, geochemical and geophysical monitoring. Melt inclusions: methods, applications and problems, 26–30 September, Seiano di Vico Equense (near Napoli), Italy, pp 211–216
Thomas R, Klemm W (1997) Microthermometric study of silicate melt inclusions in Variscan granites from SE Germany: volatile content and entrapment conditions. J Petrol 38:1753–1765
Thomas R, Webster JD (2000) Strong Sn enrichment in a pegmatite-forming melt. Miner Deposita 35:570–582
Thomas R, Webster JD, Heinrich W (2000) Melt inclusions in pegmatite quartz: complete miscibility between silicate melts and hydrous fluids at low pressure. Contrib Miner Petrol 139:394–401
Thomas R, Förster H-J, Heinrich W (2003) The behaviour of boron in a peraluminous granite–pegmatite system and associated hydrothermal solutions: a melt and fluid-inclusion study. Contrib Miner Petrol 144:457–472
Tischendorf G (1988) On the genesis of tin deposits related to granites: the example Erzgebirge. Z Geol Wissen 16:407–420
Veksler I IV, Thomas R (2002) An experimental study of B-, P- and F-rich synthetic granite pegmatite at 0.1 and 0.2 GPa. Contrib Miner Petrol 143:673–683
Veksler I IV, Thomas R, Schmidt CH (2002) Experimental evidence of three coexisting immiscible fluids in synthetic granitic pegmatite. Am Miner 87:775–779
Wallace PJ, Anderson AT Jr, Davis AM (1999) Gradients in H_2O, CO_2, and exsolved gas in a large-volume silicic magma system: interpreting the record preserved in melt inclusions from the Bishop Tuff. J Geophys Res 104(B9):20097–20122

Webster JD, Duffield WA (1994) Extreme halogen abundances in tin-rich magma of the Taylor Creek rhyolite, New Mexico. Econ Geol 89:840–850

Webster JD, Rebbert CR (2001) The geochemical signature of fluid-saturated magma determined from silicate melt inclusions in Ascension Island granite xenoliths. Geochim Cosmochim Acta 65:123–136

Webster JD, Thomas R, Rhede D, Förster H-J, Seltmann R (1997) Melt inclusions in quartz from an evolved peraluminous pegmatite: geochemical evidence for strong tin enrichment in fluorine-rich and phosphorus-rich residual liquids. Geochim Cosmochim Acta 61:2589–2604

Webster JD, Raia F, Tappen C, DeVivo B (2003) Pre-eruptive geochemistry of the ignimbrite-forming magmas of the Campanian Volcanic Zone, Southern Italy, determined from silicate melt inclusions. Miner Petrol 79:99–125

Webster J, Thomas R, Förster H-J, Seltmann R, Tappen C (2004) Geochemical evolution of halogen-enriched, granite magmas and mineralizing fluids of the Zinnwald tin-tungsten mining district, Erzgebirge, Germany. Miner Deposita 39:452–472